Human Lung Conventional Dendritic Cells Orchestrate Lymphoid Neogenesis During COPD

Thomas Naessens[1], Yannick Morias[2*], Eva Hamrud[1*], Ulf Gehrmann[1], Ramachandramouli Budida[1], Johan Mattsson[1], Tina Baker[3], Gabriel Skogberg[4], Elisabeth Israelsson[1], Kristofer Thörn[1], Martijn J. Schuijs[5], Bastian Angermann[1], Faye Melville[6], Karl J Staples[6], Danen M Cunoosamy[1#], Bart N Lambrecht[7,8,9#]

Affiliations

[1]Translational Science and Experimental Medicine, Research and Early Development, Respiratory, Inflammation, Autoimmunity, BioPharmaceuticals R&D, AstraZeneca, Gothenburg, Sweden

[2]Bioscience Cardiovascular, Research and Early Development, Cardiovascular, Renal and Metabolism (CVRM), BioPharmaceuticals R&D, AstraZeneca, Gothenburg, Sweden

[3]Translational Science and Experimental Medicine, Research and Early Development, Respiratory, Inflammation, Autoimmunity, BioPharmaceuticals R&D, AstraZeneca, Cambridge, UK

[4]Bioscience COPD/IPF, Research and Early Development, Respiratory, Inflammation, Autoimmunity, BioPharmaceuticals R&D, AstraZeneca, Gothenburg, Sweden

[5]Cancer Research UK Cambridge Institute, University of Cambridge, Cambridge, UK

[6]University of Southampton, Faculty of medicine, Clinical and Experimental Sciences, Southampton, United Kingdom of Great Britain and Northern Ireland

[7]Laboratory of Immunoregulation, VIB-UGhent Center for Inflammation Research, Ghent, Belgium

[8]Department of Internal Medicine and Pediatrics, Ghent University, Ghent, Belgium

[9]Department of Pulmonary Medicine, Erasmus University Medical Center, Rotterdam, The Netherlands

*Yannick Morias and Eva Hamrud contributed equally to this paper

#Danen Cunoosamy and Bart Lambrecht co-supervised the study

All correspondence to Thomas Naessens: Pepparedsleden 1, 431 50 Mölndal (Gothenburg), Sweden; Thomas.Naessens@AstraZeneca.com

M.J.S. was supported by an EMBO long-term post-doctoral fellowship (ALTF 423-2017)

Author contributions: T.N., K.J.S., D.M.C., and B.N.L. designed experiments, T.N., Y.M., E.H., U.G., J.M., R.B., M.J.S., G.S., K.T. and F.A. performed experiments. T.N., E.H., U.G., T.B., E.I. and B.A. analyzed data. T.N., D.M.C, and B.N.L. wrote the manuscript with input from all co-authors.

Running head: Lung cDC2 drive lymphoid neogenesis during COPD.

Descriptor number: 9.13 COPD: Pathogenesis

Total word count: 4136

This article has an online data supplement, which is accessible from this issue's table of content online at www.atsjournals.org.

At a Glance Commentary

Scientific Knowledge of on the Subject

Chronic obstructive pulmonary disease (COPD) severity and tissue destruction correlate with the development of tertiary lymphoid organs (TLO). T follicular helper (Tfh)-cells represent a specialized $CD4^+$ T-cell subset, key for lymphoid organ formation. Dendritic cells (DC) are potent inducers of $CD4^+$ T-cell responses, including Tfh-cell responses. However, how human lung DC polarize Tfh-cells during COPD and hence contribute to the generation of TLOs remains to be elucidated.

What this Study Adds to the Field

Single cell RNA sequencing showed that the myeloid cell compartment in the human non-obstructed lung is highly heterogeneous, containing multiple DC and monocyte/macrophage subsets. Among these, $CD1c^+$ conventional (c)DC (cDC2) were the most potent inducers of Tfh-cell polarization. Importantly, compared to cDC2 from non-obstructed control lungs, cDC2 derived from COPD lungs showed increased potential to polarize Tfh-cells. Mechanistically, cDC2 exhibited a unique migratory signature, including expression of the oxysterol receptor EBI2, known to control spatial organization of immune cells in TLO. Furthermore, we demonstrated the crucial contribution of the OX40-OX40L co-stimulatory axis to cDC2 mediated Tfh-cell induction. Additionally, cDC2 exhibited (transcriptional) expression of several other pathways and genes related to DC-induced Tfh-priming. Together, our study revealed a novel immune mechanism underlying TLO formation during COPD pathogenesis.

Impact: Our study reveals a new (immune) mechanism underlying TLO formation during COPD and argues for increased investigation of the role of this pathway, and TLO formation in general, in COPD pathogenesis and progression. In addition, the data provide conceptual

advances regarding the formation of TLO during other respiratory and non-respiratory diseases and contribute to the field of human lung dendritic cells and T follicular helper cells.

Abstract

Rationale: Emerging evidence supports a crucial role for tertiary lymphoid organs (TLOs) in chronic obstructive pulmonary disease (COPD) progression. However, mechanisms of immune cell activation leading to TLO in COPD remain to be defined.

Objectives: To examine the role of lung dendritic cells (DC) in T follicular helper (Tfh)-cell induction, a T-cell subset critically implicated in lymphoid organ formation, in COPD.

Methods: Myeloid cell heterogeneity and phenotype was studied in an unbiased manner via single-cell RNA sequencing on HLA-DR$^+$ cells sorted from human lungs. The *in vitro* capability of FACS-sorted DC-subsets of control and COPD lungs to polarize IL-21$^+$CXCL13$^+$ Tfh-like cells was measured. *In situ* imaging analysis was performed on COPD stage IV GOLD lungs with TLO.

Measurements and Main Results: ScRNAseq analysis revealed a high level of heterogeneity among human lung myeloid cells. Among these, cDC2 showed increased induction of IL-21$^+$CXCL13$^+$ Tfh-like cells. Importantly, the capacity to induce IL-21$^+$ Tfh-like cells was higher in cDC2s from COPD patients compared with control patients. Increased Tfh-induction by COPD cDC2 correlated with increased presence of Tfh-like cells in COPD lungs as compared to controls, and cDC2 co-localized with Tfh-like cells in TLOs of COPD. Mechanistically, cDC2 exhibited a unique migratory signature and (transcriptional) expression of several pathways and genes related to DC-induced Tfh-priming. Importantly, blocking the co-stimulatory OX40L-OX40 axis reduced Tfh-induction by control lung cDC2.

Conclusions: In COPD lung, we found lung EBI2$^+$ OX-40L-expressing cDC2 that induces IL-21$^+$ Tfh-like cells, suggesting an involvement of these cells in TLO formation.

Abstract word count: 247

Introduction

Chronic obstructive pulmonary disease (COPD) is currently the third leading cause of death worldwide (1) and is characterized by progressive airway inflammation, emphysema and impaired lung function resulting from inhaled oxidants such as cigarette smoke (CS). COPD severity and tissue destruction correlate with development of tertiary lymphoid organs (TLO) (2, 3). While rarely developing in healthy individuals, lung TLO formation is significantly increased in COPD (GOLDI/II) patients (4). Finally, in severe/end-stage COPD patients (GOLD III/IV), TLO numbers and size further increase and can be found in nearly 50% of the small airways (2, 4). TLOs consist of well-defined B-cell follicles surrounded by T-cells interspersed with dendritic cells (DC), reminiscent of the structural organization also seen in secondary lymphoid organs (5). Several studies have shown that absence of TLOs via either use of B-cell deficient mice (6) or antibodies blocking B-cell recruitment (7) or survival (4, 8), prevented CS-induced emphysema in a murine COPD model. However, mechanisms governing TLO formation during COPD remain to be elucidated.

Peripheral T follicular helper (Tfh-)like cells exhibit phenotypic overlap with 'bona fida' Tfh-cells and regulate local B-cell isotype switching in peripheral diseased organs, including skin (9), synovial tissue (10) and lung (11) via IL-21 secretion. Importantly, we and others have also described the presence of IL-21$^+$ Tfh-like cells in TLO of idiopathic pulmonary arterial hypertension (IPAH) (12) and COPD (3) lungs, suggesting these cells are involved in TLO formation and maintenance.

Human DC are heterogeneous and consists of different subsets, including two conventional (c)DC populations (CD141$^+$ cDC1 and the CD1c$^+$ cDC2) and plasmacytoid (p)DC (13, 14). It has been shown that mice, in which DC were depleted, failed to develop and maintain lung TLO in response to allergens or virus infection (15-17). In contrast, repeated

pulmonary delivery of activated DC was sufficient to induce TLO formation (15, 18). These studies highlight a crucial role for DC in TLO formation and maintenance. However, how DC induce TLO, especially during COPD, is unknown.

We hypothesized that human lung DC induce Tfh-like cell polarization and hence contribute to subsequent lymphoid neogenesis during COPD. We first used an unbiased approach to address the complexity of Lineage(Lin)$^-$HLA-DR$^+$ lung cells and found a high level of heterogeneity. We then demonstrated that cDC2 are the most efficient subset in inducing IL-21$^+$ Tfh-like cells. Importantly, cDC2 isolated from COPD lungs showed increased potential to polarize Tfh-like cells. Mechanistically, we found that cDC2 expressed a unique migratory signature, suggesting these cells are highly capable to migrate to the site of TLO formation and subsequently interact with CD4$^+$ T-cells. Furthermore, blocking the co-stimulatory OX40L-OX40 axis reduced Tfh-induction by cDC2 derived from non-obstructed control lungs. Some of the results have been previously reported in the form of an abstract (19).

Methods

Detailed description of materials and methods can be found in the online methods supplement.

Human lung samples

Lung samples were obtained from non-obstructed control or COPD subjects. Study and consent procedures were reviewed and approved by the Swedish Research Ethical Committee in Gothenburg, Sweden (FEK 675-12/2012 and 1026-15, March 2016) in accordance with the principles of the Declaration of Helsinki. Written informed consent was obtained preoperatively. Table 1 shows demographics and lung function. Additional information about the source and processing of the human lung tissue samples is described in the online methods supplement.

In vitro *DC/T-cell co-cultures*

Mixed Leukocyte Reactions (MLR) were set up between FACS-sorted lung DC populations and allogeneic naïve blood $CD4^+$ T-cells as described in the online supplement. T-cell proliferation and polarization, including cytokine and transcription factor profiling, were subsequently analyzed via flow cytometry as described in the online supplement.

Ex vivo *phenotyping of lung leukocyte populations*

Flow cytometry was used to assess expression of extracellular and intracellular phenotypic protein markers by lung DC and T-cell subsets as described in the online supplement. Single-cell RNA transcriptomes of the lung HLA-DR^+ fraction were generated and analyzed as described in the online supplement.

In situ *imaging of GOLD IV COPD lung TLO*

To image *CH25H* and *CD19* mRNA topography in the lung TLO, RNAScope was performed as described in the online supplement. Fluorescence microscopy was used to determine the presence and anatomical localization of cDC2 in lung TLO as described in the online supplement.

Results

Unbiased single cell RNA sequencing analysis of human lung Lin^-HLA-DR^+ cells.

Myeloid cells represent a heterogeneous population and comprise several subtypes (14). To date, definition of human lung myeloid cells was biased by the limited markers available to identify and isolate the cells. To identify the different myeloid cell populations in the human lung in an unbiased way, we performed single-cell RNA sequencing on Lin^-HLA-DR^+ cells from non-obstructed lungs. Different DC (including cDC1, cDC2 and pDC) and monocyte subsets (including $CD14^+$, $CD16^+$ and $CD14^+CD16^+$ monocytes) were

FACS-sorted based on the expression of DC and monocyte subset defining surface markers (Figure E1A) (14) and pooled afterwards in enriched proportions before sequencing.

Unsupervised clustering identified 14 clusters (Figure 1A). Differential gene expression between clusters was analyzed (Figure 1B). Cluster 1 highly expressed cDC2-associated genes such as *CD1C*, *CLEC10A*, *FCER1A* and *CD1A*. Cluster 2 highly expressed monocyte/macrophage-related genes such as *MRC1, CTSD, MARCO and VSIG4* while cluster 3 is characterized by cell cycle gene expression, including *TOP2A*, *CENPF1* and *STMN1*. Cluster 4 expressed high levels of pDC-associated genes, including *TCF4*, *GZMB*, *CLEC4C* and *BCL11A* while cluster 5 exhibited high expression levels of monocyte/macrophage-related genes, including *S100A8*, *S100A9*, *FCN1* and *VCAN*. Cluster 6 expressed natural killer (NK) cell-associated genes, like *GZMA*, *CD96* and *GNLY* while cluster 7 displayed expression of monocyte/macrophage-related genes, including *FCGR3A*, *CTSS*, *PECAM1* and *MAFB*. Cluster 8 expressed high levels of cDC1 genes, including *CLEC9A*, *IRF8*, *ID2* and *XCR1*. Cluster 9 exhibited expression of type II alveolar epithelial cells (AEC), including *SFTPC*, *SFTPB*, *SFTPD* and *EPCAM*. Cluster 10 expressed endothelial cell-related genes including *VWF*, *CAV1* and *GIMAP7*. Furthermore, both cluster 9 and cluster 10 lack expression of the pan-leukocyte marker gene *PTPRC* (coding for CD45), further confirming their non-immune cell nature (Figure E1B). Cluster 11 highly expressed genes associated with DC activation, including *CCR7*, *CCL22*, *LAMP3* and *BIRC3*. Both cluster 12 and cluster 14 expressed monocyte/macrophage-related genes, like *CXCL10*, *CXCL11*, *CCL8* and *GBP1* for cluster 12 and *LYVE1*, *C1QA*, *CD163* and *CD14* for cluster 14. Finally, cluster 13 exhibited expression of mast cell genes, including *KIT*, *CPA3* and *MS4A2*. The complete list of top 20 differentially expressed genes is available in Table S1.

To confirm the identity of the different clusters, we calculated signature scores for each single cell using published transcriptome signatures for human blood (20) and lung

(21) leukocyte subsets (Figure 1C). Cluster 1 had the highest score for the cDC2 signature while cluster 2 exhibited score increase for $CD14^{++}CD16^{+}$ monocyte and $CD14^{+}$ and $CD16^{+}$ monocyte cell signatures. Cluster 3 showed an overlap with a signature defining a proliferating monocyte/macrophage (Mac/mono cycl.) subset as observed in (21). Cluster 4 displayed a clear overlap with the pDC signature while cluster 5 exhibited a high score for the $CD14^{+}$ monocyte and $CD14^{+}CD16^{+}$ monocyte signature. Cluster 6 overlapped with the NK cell signature and cluster 7 with the $CD16^{+}$ monocyte and $CD14^{++}CD16^{+}$ monocyte cell signature. Cluster 8 showed a clear overlap with the cDC1 signature while cluster 9 and cluster 10 overlapped with signatures of type II AEC and endothelial cells respectively. For cluster 11, we observed a high overlap with an 'activated DC' signature. As expected, both cluster 12 and cluster 14 had high signature scores for macrophage phenotypes (mac1 and mac2 respectively) observed earlier in the lung (21). Finally, cluster 13 had a high score for a mast cell signature.

Based on the relevance in terms of their potency to prime T-cell activation and polarization we opted to primarily focus on cDC2, cDC1 and pDC, rather than on macrophage subsets, NK-cells, mast cells and structural cells for the rest of the study. All monocyte subsets are weak stimulators of naïve T-cells (22). Therefore, we finally opted to include only $CD14^{+}$ monocytes as a reference monocyte population as these cells embody the 'classical' monocyte subset (22). Single-cell transcriptome data confirmed that cDC1, cDC2, pDC and $CD14^{+}$ monocytes each represent homogeneous cell populations. Furthermore, cells in the 'activated DC' cluster expressed cDC2 and cDC1 hallmark genes, including *CD1c* and *IRF8* respectively (Figure E1B). Therefore, this cluster represented a mixture of cDC1 and cDC2 with a distinct activation status rather than a separate DC subset with a distinct ontogeny.

However, additional flow cytometry analysis revealed heterogeneous expression of several myeloid cell markers by cDC2, including FcεRI, CD1a and the monocyte marker CD14 (Figure E1C). This could imply potential presence of a $CD14^{hi}Fc\varepsilon RI^{hi}CD1a^{hi}$ monocyte-

derived (mo)DC population within the cDC2 gate. However, $CD14^{lo}$ and $CD14^{hi}$ cDC2 fractions displayed a similar heterogeneous expression pattern of both FcεRI and CD1a, hence we couldn't identify a clear $CD14^{hi}FcεRI^{hi}CD1a^{hi}$ subset (Figure E1D). Moreover, $CD14^{lo}$ and $CD14^{hi}$ fractions exhibited a similar (cDC2) expression profile of the lineage-defining transcription factors IRF4 and IRF8 (14), clearly distinct from that exhibited by $CD14^{+}$ monocytes, considered as the precursors of moDC (14) (Figure E1D). Thus, there were no immediate indications that the $CD14^{+}$ cDC2 represent an ontogenetically different subset. Moreover, full comprehension of the ontogenetic relationship between $CD14^{lo}$ and $CD14^{hi}$ cDC2 fractions requires further investigation and is beyond the scope of this study. Therefore, we decided to isolate the different lung DC subsets as outlined in Figure E1A.

Lung cDC2 are the most potent subset to polarize naïve $CD4^{+}$ T-cells into Tfh-like cells

To assess the capacity of the different human lung DC subsets to polarize naïve $CD4^{+}$ T-cells into Tfh- or Tfh-like cells, FACS-sorted lung DC subsets were co-cultured with allogeneic naïve blood $CD4^{+}$ T-cell (MLR). The degree of Tfh-polarization was assessed at d7 of the culture. Compared to other DC subsets, cDC2 induced the highest proportion of $CD4^{+}$ T-cells expressing high levels of ICOS and PD-1, two hallmark Tfh-markers (Figure 2A and E2A). Of note, lung pDCs and $CD14^{+}$ monocytes are poor stimulators of naïve $CD4^{+}$ T-cell proliferation (Figure E3A), underlying the lower proportions of $ICOS^{hi}PD\text{-}1^{hi}$ T-cells in these co-cultures. However, cDC2 and cDC1 induced similar levels of T-cell proliferation (Figure E3A) implying that there was an intrinsic qualitative difference between both cDC subsets to promote Tfh-like cell skewing. Compared to $ICOS^{-}PD\text{-}1^{+}$, $ICOS^{+}PD\text{-}1^{-}$ and $ICOS^{-}PD1^{-}$ T-cell subsets in the co-culture, $ICOS^{hi}PD\text{-}1^{hi}$ T-cells were characterized by the highest surface levels of OX40, another critical Tfh-cell marker (Figure 2B). Moreover, compared to the three other T-cell populations, $ICOS^{hi}PD\text{-}1^{hi}$ T-cells were the dominant producers of IL-21 and CXCL13, the hallmark Tfh cytokine and chemokine respectively, confirming the Tfh-like cell nature of

this T-cell population (Figure 2C and E2B). In contrast, there was no significant difference in secretion of the Th1 cytokine IFN-γ by ICOS^{hi}PD-1^{hi} T-cells as compared to ICOS^{-}PD-1^{+} T-cells (Figure E3B), demonstrating that the ICOS^{hi}PD-1^{hi} T-cells do not simply represent a generally increased activation state. Importantly, compared to cDC1, lung cDC2 induced increased proportions of ICOS^{hi}PD-1^{hi} IL-21 secreting T-cells (Figure 2D). Of note, there was no significant difference in the induction of IFN-γ secretion by ICOS^{+}PD-1^{+} T-cells induced by cDC1 and cDC2, implying a degree of selectivity in the T-cell cytokine responses elicited by cDC2 versus cDC1 (Figure E3C).

To further confirm the induction of Tfh-cells in the co-cultures, we analyzed expression of CXCR5, a classical Tfh-cell surface marker, and Bcl6, key transcription factor driving Tfh-cell development (23). Expression of CXCR5 was transient and not detectable at day 7 (*data not shown* and (24)). Therefore, we determined the proportion of CXCR5^{hi}ICOS^{hi}PD-1^{hi}Bcl6^{hi} Tfh-like cells in the different co-cultures at day 4, a time point that corresponds with peak CXCR5 expression (24). In line with our previous results from day 7, cDC2 were the most efficient inducers of ICOS^{hi}CXCR5^{hi} T-cells as compared to cDC1, pDC and CD14^{+} monocytes (Figure 2E and E2C). Importantly, in contrast to ICOS^{+}CXCR5^{-} and ICOS^{-}CXCR5^{-}, ICOS^{hi}CXCR5^{hi} T-cells were almost exclusively PD-1^{hi}Bcl6^{hi}, further supporting their Tfh-like nature (Figure 2F and E2D).

Collectively, these results demonstrate that human resident lung cDC2 are the most potent DC subset to polarize Tfh-like cells from naïve CD4^{+} T-cells.

cDC2 from GOLD II COPD lungs show increased potential to induce Tfh-like cells, which correlated with increased presence of Tfh-like cells in the lung tissue

We next assessed whether lung cDC2 from COPD patients exhibited an increased capacity to induce Tfh-like cells as compared to cDC2 from non-obstructed lungs. To this end,

we isolated cDC2 from GOLD II COPD peripheral lung tissue and co-cultured these cells with allogeneic naïve blood $CD4^+$ T-cells. COPD lung cDC2 induced increased proportions of Tfh-like cells as compared to control cDC2 from non-obstructed lungs (Figure 3A and E4A). Importantly, Tfh-like cells induced by COPD cDC2 contained an increase in the frequency of IL-21^+ cells as compared to Tfh-like cells induced by cDC2 from non-obstructed lungs (Figure 3B and E4B). Of note, the difference in Tfh-like cell induction between COPD and control cDC2 could not be attributed to a difference in their potential to stimulate T-cell proliferation (Figure E4C). Furthermore, control and COPD cDC2 contained a similar proportion of $CD14^{hi}$ cells, indicating that a difference in $CD14^{hi}$ cDC2 fraction did not underlie the difference in Tfh-like cell induction by control and COPD cDC2 (Figure E4D).

We next investigated whether there is a corresponding increased presence of Tfh-like cells in peripheral lung tissue of GOLD II COPD subjects. Flow cytometry analysis revealed the presence of $ICOS^{hi}PD\text{-}1^{hi}$ T-cells in both control and COPD lung tissue. Importantly, compared to control lungs, the frequency of $ICOS^{hi}PD\text{-}1^{hi}$ T-cells was increased GOLD II COPD lungs (Figure 3C and E4D). In line with our *in vitro* findings, lung $ICOS^{hi}PD\text{-}1^{hi}$ T-cells were the dominant IL-21 producers as compared to $ICOS^{-}PD\text{-}1^{hi}$, $ICOS^{hi}PD\text{-}1^{-}$ and $ICOS^{-}PD\text{-}1^{-}$ T-cell fractions, confirming the Tfh-like nature of these cells (Figure 3D).

Lung cDC2 express a unique migratory signature distinct from cDC1

The chemoattractants CXCL12 and CXCL13 are instrumental for TLO-formation during COPD by mediating the recruitment and localization of the critical cell types, including T cells, B cells and DCs (7, 25, 26). Therefore, we analyzed expression of the corresponding receptors CXCR4 and CXCR5 on cDC2 and cDC1 via flow cytometry. In control lungs, cDC2 tended to exhibit increased expression of CXCR5 while CXCR4 levels were significantly increased as compared to cDC1 (Figure 4A and E5A). However, there was

no difference in CXCR5 and CXCR4 expression between control and COPD cDC2 (Figure E5B).

In addition, 7α,25-dihydroxycholesterol, a cholesterol derivative, is a key chemoattractant in organizing the lymphoid microenvironment (27). The receptor for 7α,25-dihydroxycholesterol, EBI2 (GPR183) is expressed on a variety of leukocytes, including T-cells, B-cells, ILC3 and DC (27). Importantly, the oxysterol-EBI2 axis was recently shown to be a key regulator of lung TLO formation in a mouse model of COPD (28). Moreover, EBI2 controls cDC2 positioning at the B-T zone border of mouse lymphoid organs (29). In non-obstructed lungs, cDC2 expressed increased EBI2 surface levels as compared to cDC1 (Figure 4A). Of note, control and COPD cDC2 displayed similar expression levels of EBI2 (Figure E5B). Additionally, we investigated the expression of EBI2 on T cell subsets in the peripheral lung tissue in control and COPD subjects. Compared to $ICOS^{-}PD\text{-}1^{hi}$, $ICOS^{hi}PD\text{-}1^{-}$ and $ICOS^{-}PD\text{-}1^{-}$ lung T-cells, the dominant IL-21 producing $ICOS^{hi}PD\text{-}1^{hi}$ T-cell fraction displayed the highest levels of surface EBI2 as well (Figure 4B and E5C).

To further study the association between the oxysterole-EBI2 axis and TLO-formation in COPD, we analyzed a publicly available dataset containing total lung transcriptome data from a cohort of COPD patients (GOLD I – IV) and healthy control subjects (Figure 4C) (GSE47460 derived from lung samples obtained through the NHLBI-funded Lung Tissue Research Consortium (LTRC) as part of the Lung Genomic Research Consortium (LGRC)). mRNA transcripts encoding *EBI2* and mRNA encoding enzymes in the cholesterol metabolic pathway (i.e. *CH25H*, *CYP1B1* and *CYP7B1*) positively correlated with COPD disease stage and hence inversely correlated with %FEV1 (Figure 4C). Importantly, lung *EBI2*, *CH25H*, *CYP1B1* and *CYP7B1* mRNA expression all correlated with *CXCL13* mRNA expression, a marker for TLO formation during COPD disease (Figure 4C). Finally, lung *CH25H* mRNA strongly correlated with *EBI2* mRNA levels (Figure 4D).

The correlation between the oxysterole-EBI2 axis and TLO-formation encouraged us to investigate the presence of the cholesterol metabolic pathway in TLOs of end-stage (GOLD IV) COPD patients. Indeed, RNAscope analysis of lung TLOs confirmed the expression of *CH25H* mRNA, encoding for one of the upstream enzyme involved in cholesterol degradation (27) in both the B cell follicular area and the T cell zone of the TLO (Figure 4E).

Finally, we performed confocal imaging of GOLD IV COPD lung tissue to determine the anatomical localization of cDC2 in the TLOs. This immunofluorescence analysis showed that cDC2 were indeed abundantly present in the follicular T cell zone of the TLOs, linking the unique migratory signature of cDC2 to the actual presence of these cells to TLOs during COPD (Figure 5).

Lung cDC2 express increased levels of OX40L and transcriptional signatures related to Tfh-cell priming

To gain insights into the mechanism used by cDC2 to induce Tfh-like cells, we performed flow cytometric analysis of the co-stimulatory repertoire expressed on the different lung DC subsets. ICOSL, PDL1 and OX40L are known to deliver critical co-stimulatory signals to skew naïve T cells into Tfh-cells (23, 24). In non-obstructed control lungs, cDC2 and cDC1 subsets expressed similar levels of ICOSL and PDL1. However, we observed a significant increase in OX40L expression in cDC2 cells as compared to cDC1 (Figure 6A). Importantly, compared to control cDC2s, OX40L levels were even further increased on COPD cDC2 (Figure 6B). We next investigated whether OX40L was involved in Tfh-like cell polarization by lung cDC2. cDC2 isolated from non-obstructed control lung tissue were co-cultured with allogeneic naïve $CD4^+$ T-cells in the presence of a blocking antibody for OX40L (oxelumab) or IgG isotype control. $ICOS^+PD\text{-}1^+$ Tfh-like cell priming was analyzed at d7 of

the co-culture. Compared to the IgG control, blocking OX40L reduced $ICOS^{+}PD\text{-}1^{+}$ Tfh-like cell induction in each experiment (Figure 6C), confirming the importance of the OX40L-OX40 axis.

To further understand the mechanisms underlying the enhanced ability of cDC2 to polarize Tfh-like cells, we compared the transcriptional profile of cDC2 with cDC1. cDC2 and cDC1 were FACS-sorted and their transcriptomic profile was generated via Next Generation Sequencing (NGS). Interestingly, this analysis revealed that genes encoding for signaling components of the IL-6 ($p = 0{,}0002$) and IL-1 ($p = 0{,}02$) pathways, critical for Tfh-cell development (30, 31), were significantly upregulated in cDC2 (Figure 6D). Furthermore, transcripts involved in general DC maturation and activation, features of DC contributing to Tfh generation (32) were also upregulated in cDC2 compared to cDC1 (Figure 6D). Consistent with these observations, biocomputational analysis identified signaling through CD40 ($p = 1{,}15 \times 10^{-10}$); secretion of multiple effector cytokines such as TNF ($p = 1{,}58 \times 10^{-22}$), IL-1β ($p = 6{,}01 \times 10^{-21}$), IL-6 ($p = 2{,}86 \times 10^{-8}$) and IL-18 ($p = 9{,}43 \times 10^{-5}$) and transcription factors and signaling mediators like NF-κB ($p = 4{,}36 \times 10^{-14}$), STAT3 ($p = 4{,}06 \times 10^{-10}$) and ID3 ($p = 5{,}96 \times 10^{-5}$) as putative upstream regulators of transcriptional signatures in lung cDC2 (Figure 6E). In contrast, transcriptional pathways and genes downregulated in cDC2 had no immediate connection to Tfh-priming by DC or were negatively associated with Tfh polarization, eg. LXR ($p = 9{,}54 \times 10^{-5}$) (33) (Figure 6E). Collectively, transcriptomic analysis indicates that lung cDC2 are characterized by signatures related to key pathways involved in Tfh- or Tfh-like cell polarization.

Discussion

The current study reveals a potent ability for cDC2 to induce IL-21 and CXCL13 secreting Tfh-like cells, suggesting a crucial role for cDC2 in TLO formation during COPD.

ScRNA-seq revealed a high level of heterogeneity among human lung $Lin^-HLA\text{-}DR^+$ cells. In agreement with previous studies investigating human blood and lung tumor myeloid cell heterogeneity (20, 21), we identified clusters of cDC1, cDC2, pDC, a cluster containing 'activated DC', the three monocyte subsets, being $CD14^+$ ('classical') monocytes, $CD16^+$ ('non-classical') monocytes and $CD14^{++}CD16^+$ ('intermediate') monocytes and several additional monocyte/macrophage populations. Furthermore, we found a population of NK-cells, mast cells, type II AEC and endothelial cells. HLA-DR expression by NK-cells and mast cells was reported previously (34, 35). Although type II AEC and endothelial cells can express HLA-DR (36, 37) we believe that these rather represented a minor contamination. Compared to the Zilionis *et al.* study, we found less monocyte/macrophage populations/phenotypes in the lung tissue. This discrepancy could be explained by the fact that alveolar cells, containing multiple alveolar macrophage phenotypes, were not part of our analysis. Furthermore, we sampled lung tissue distant from the tumor bed, likely lacking several tumor-infiltrating myeloid cell populations (TIMs) (21). Finally, this dataset has some limitations that warrant future investigations, notably the lack of a larger validation cohort, the relatively low numbers of cells analyzed and the read-depth which might have limited the power to define lung cell subsets in this experiment.

The role of DC during COPD remains controversial. Several studies demonstrated that DC exhibit an increased co-stimulatory repertoire (38) and that, especially $CD1c^+$ DC (cDC2), drive Th17-responses during cigarette smoke induced lung emphysema in both humans and mice (39-42). In contrast, a recent report stated that human lung $CD1c^+$ DC displayed a regulatory function during COPD, suppressing pathogenic T-cell responses and inducing regulatory T-cells (43). In our study, compared to other DC subsets, cDC2 were the most potent in skewing naïve $CD4^+$ T-cells into IL-21 and CXCL13 secreting Tfh-like cells. These findings are in line with a recent murine study, demonstrating that lung cDC2, but not

cDC1, were driving antigen-specific Tfh-induction (44). Furthermore, recent research showed that human tonsil cDC2 were the most efficient in Tfh-cell polarization as well (45). Strikingly, by using lung resident cDC2 in our study, we also demonstrated that human cDC2 residing in non-lymphoid peripheral organs can induce Tfh-like cells without requirement of prior migration to draining lymph nodes.

The increased capability of COPD cDC2 to induce Tfh-like cells was associated with increased presence of Tfh-like cells in the COPD parenchyma. To our knowledge, we are the first to demonstrate the presence of a Tfh-like cell during early (GOLDI/II) stages of COPD. We and others showed already the presence of peripheral, extrafollicular IL-21 secreting PD-1^{+}ICOS^{+} Tfh-like cells, that lack CXCR5 and/or Bcl6 expression, in rheumatoid arthritis (10), skin fibrosis (9) and an HDM-driven asthma model (11). The effect of Tfh-like cells on COPD development and progression remains to be elucidated. However, Ladjemi *et al* recently confirmed the presence of IL-21^{+} T-cells that did not co-express CXCR5 in the TLOs of late-stage COPD lungs, further supporting a role for an extrafollicular Tfh-like cell type and IL-21 (3).

cDC2 exhibited a unique migratory signature, including increased expression of CXCR4, CXCR5 and EBI2, suggesting that these cells efficiently migrate to the site of TLO formation during COPD. Levels of CXCL12 and CXCL13, ligands for CXCR4 and CXCR5 respectively, are increased in human COPD lungs (7, 25, 26). A recent study also highlighted the crucial role of the oxysterol-EBI2 axis in COPD TLO formation (28). We now demonstrated the presence of *CH25H* mRNA in both T- and B-cell zone of TLOs during late-stage COPD. These results imply that cholesterol metabolism is important for maintaining the structure of established TLO as well by continuously recruiting T-, B-cells and cDC2. In line with this premise, we were able to detect cDC2 in the T-cell zone of GOLD IV COPD lung TLO. This observation indicates that cDC2 are also important for maintaining established

TLOs most likely via sustained antigen-presentation and induction of T(fh-like) cell polarization and proliferation.

Furthermore, we found that, compared to cDC1, cDC2 exhibited increased (transcriptional) expression of pathways and genes related to DC-induced Tfh-priming, including OX40L. In agreement with previous reports (24, 46), we confirmed that the OX40L-OX40 axis promoted human Tfh-polarization. Mediators that stimulate OX40L expression, including TSLP, IL-1, IL-33 and GM-CSF, are abundantly present in the lung (47, 48) and elevated levels are observed in COPD subjects (47, 49, 50), likely underlying the increased OX40L levels expressed by COPD cDC2. Additionally, several genes encoding for cytokine mediators that deliver Tfh-skewing signals, including IL-6, IL-1β and TGFβ have already been shown to be increased during COPD (51). This implies that these signals might further expand the cDC2-induced Tfh-like cell polarization during COPD.

Collectively, we propose a model (Figure 7) in which, during COPD, locally produced chemokines, like CXCL12 and CXCL13, and cholesterol metabolites attract cDC2 and $CD4^+$ T-cells to the site of TLO formation. Upon encounter, cDC2 skew IL-21^+ Tfh-like cell polarization via OX40L and cytokine signals. Finally, the chronicity of this self-amplifying loop results in the formation of well-organized TLOs in which Tfh-like cell clonality and proliferation is further sustained by cDC2. Thus, our study reveals a new (immune) mechanism underlying TLO formation during COPD. However, additional studies will be required to fully comprehend the role of this pathway, and of TLO formation in general, in COPD pathogenesis and progression.

Acknowledgments

We are grateful to all the lung tissue donors. We thank the surgeons and nurses from the Thoraxkliniken, Sahlgrenska University Hospital and Gothenburg University, Gothenburg,

Sweden for sample collection. We also wish to thank Mr Aiman Alzetani, Professor Christian Ottensmeier and the rest of the Target Lung team for sample collection in Southampton.

References

1. Collaborators GBDCoD. Global, regional, and national age-sex specific mortality for 264 causes of death, 1980-2016: a systematic analysis for the Global Burden of Disease Study 2016. *Lancet* 2017; 390: 1151-1210.

2. Hogg JC, Chu F, Utokaparch S, Woods R, Elliott WM, Buzatu L, Cherniack RM, Rogers RM, Sciurba FC, Coxson HO, Pare PD. The nature of small-airway obstruction in chronic obstructive pulmonary disease. *N Engl J Med* 2004; 350: 2645-2653.

3. Ladjemi MZ, Martin C, Lecocq M, Detry B, Aboubakar Nana F, Moulin C, Weynand B, Fregimilicka C, Bouzin C, Thurion P, Carlier F, Serre J, Gayan-Ramirez G, Delos M, Ocak S, Burgel PR, Pilette C. Increased IgA Expression in Lung Lymphoid Follicles in Severe COPD. *Am J Respir Crit Care Med* 2018.

4. Polverino F, Cosio BG, Pons J, Laucho-Contreras M, Tejera P, Iglesias A, Rios A, Jahn A, Sauleda J, Divo M, Pinto-Plata V, Sholl L, Rosas IO, Agusti A, Celli BR, Owen CA. B Cell-Activating Factor. An Orchestrator of Lymphoid Follicles in Severe Chronic Obstructive Pulmonary Disease. *Am J Respir Crit Care Med* 2015; 192: 695-705.

5. Randall TD. Bronchus-associated lymphoid tissue (BALT) structure and function. *Adv Immunol* 2010; 107: 187-241.

6. John-Schuster G, Hager K, Conlon TM, Irmler M, Beckers J, Eickelberg O, Yildirim AO. Cigarette smoke-induced iBALT mediates macrophage activation in a B cell-dependent manner in COPD. *Am J Physiol Lung Cell Mol Physiol* 2014; 307: L692-706.

7. Bracke KR, Verhamme FM, Seys LJ, Bantsimba-Malanda C, Cunoosamy DM, Herbst R, Hammad H, Lambrecht BN, Joos GF, Brusselle GG. Role of CXCL13 in cigarette smoke-induced lymphoid follicle formation and chronic obstructive pulmonary disease. *Am J Respir Crit Care Med* 2013; 188: 343-355.

8. Seys LJ, Verhamme FM, Schinwald A, Hammad H, Cunoosamy DM, Bantsimba-Malanda C, Sabirsh A, McCall E, Flavell L, Herbst R, Provoost S, Lambrecht BN, Joos GF, Brusselle GG, Bracke KR. Role of B Cell-Activating Factor in Chronic Obstructive Pulmonary Disease. *Am J Respir Crit Care Med* 2015; 192: 706-718.

9. Taylor DK, Mittereder N, Kuta E, Delaney T, Burwell T, Dacosta K, Zhao W, Cheng LI, Brown C, Boutrin A, Guo X, White WI, Zhu J, Dong H, Bowen MA, Lin J, Gao C, Yu L, Ramaswamy M, Gaudreau MC, Woods R, Herbst R, Carlesso G. T follicular helper-like cells contribute to skin fibrosis. *Sci Transl Med* 2018; 10.

10. Rao DA, Gurish MF, Marshall JL, Slowikowski K, Fonseka CY, Liu Y, Donlin LT, Henderson LA, Wei K, Mizoguchi F, Teslovich NC, Weinblatt ME, Massarotti EM, Coblyn JS, Helfgott SM, Lee YC, Todd DJ, Bykerk VP, Goodman SM, Pernis AB, Ivashkiv LB, Karlson EW, Nigrovic PA, Filer A, Buckley CD, Lederer JA, Raychaudhuri S, Brenner MB. Pathologically expanded peripheral T helper cell subset drives B cells in rheumatoid arthritis. *Nature* 2017; 542: 110-114.

11. Coquet JM, Schuijs MJ, Smyth MJ, Deswarte K, Beyaert R, Braun H, Boon L, Karlsson Hedestam GB, Nutt SL, Hammad H, Lambrecht BN. Interleukin-21-Producing CD4(+) T Cells Promote Type 2 Immunity to House Dust Mites. *Immunity* 2015; 43: 318-330.

12. Perros F, Dorfmuller P, Montani D, Hammad H, Waelput W, Girerd B, Raymond N, Mercier O, Mussot S, Cohen-Kaminsky S, Humbert M, Lambrecht BN. Pulmonary lymphoid neogenesis in idiopathic pulmonary arterial hypertension. *Am J Respir Crit Care Med* 2012; 185: 311-321.

13. Guilliams M, Ginhoux F, Jakubzick C, Naik SH, Onai N, Schraml BU, Segura E, Tussiwand R, Yona S. Dendritic cells, monocytes and macrophages: a unified nomenclature based on ontogeny. *Nat Rev Immunol* 2014; 14: 571-578.

14. Guilliams M, Dutertre CA, Scott CL, McGovern N, Sichien D, Chakarov S, Van Gassen S, Chen J, Poidinger M, De Prijck S, Tavernier SJ, Low I, Irac SE, Mattar CN, Sumatoh HR, Low GHL, Chung

TJK, Chan DKH, Tan KK, Hon TLK, Fossum E, Bogen B, Choolani M, Chan JKY, Larbi A, Luche H, Henri S, Saeys Y, Newell EW, Lambrecht BN, Malissen B, Ginhoux F. Unsupervised High-Dimensional Analysis Aligns Dendritic Cells across Tissues and Species. *Immunity* 2016; 45: 669-684.

15. GeurtsvanKessel CH, Willart MA, Bergen IM, van Rijt LS, Muskens F, Elewaut D, Osterhaus AD, Hendriks R, Rimmelzwaan GF, Lambrecht BN. Dendritic cells are crucial for maintenance of tertiary lymphoid structures in the lung of influenza virus-infected mice. *J Exp Med* 2009; 206: 2339-2349.

16. Muniz LR, Pacer ME, Lira SA, Furtado GC. A critical role for dendritic cells in the formation of lymphatic vessels within tertiary lymphoid structures. *J Immunol* 2011; 187: 828-834.

17. Halle S, Dujardin HC, Bakocevic N, Fleige H, Danzer H, Willenzon S, Suezer Y, Hammerling G, Garbi N, Sutter G, Worbs T, Forster R. Induced bronchus-associated lymphoid tissue serves as a general priming site for T cells and is maintained by dendritic cells. *J Exp Med* 2009; 206: 2593-2601.

18. van Rijt LS, Vos N, Willart M, Muskens F, Tak PP, van der Horst C, Hoogsteden HC, Lambrecht BN. Persistent activation of dendritic cells after resolution of allergic airway inflammation breaks tolerance to inhaled allergens in mice. *Am J Respir Crit Care Med* 2011; 184: 303-311.

19. Naessens T MY, Hamrud E, Gehrmann U, Mattsson J, Skogberg G, Israelsson E, Thörn K, Melville F, Deys L, Bracke K, Staples K, Cunoosamy D, Brusselle G, Lambrecht B. Human lung CD1c dendritic cells orchestrate lymphoid neogenesis during COPD. *ERJ* 2019.

20. Villani AC, Satija R, Reynolds G, Sarkizova S, Shekhar K, Fletcher J, Griesbeck M, Butler A, Zheng S, Lazo S, Jardine L, Dixon D, Stephenson E, Nilsson E, Grundberg I, McDonald D, Filby A, Li W, De Jager PL, Rozenblatt-Rosen O, Lane AA, Haniffa M, Regev A, Hacohen N. Single-cell RNA-seq

reveals new types of human blood dendritic cells, monocytes, and progenitors. *Science* 2017; 356.

21. Zilionis R, Engblom C, Pfirschke C, Savova V, Zemmour D, Saatcioglu HD, Krishnan I, Maroni G, Meyerovitz CV, Kerwin CM, Choi S, Richards WG, De Rienzo A, Tenen DG, Bueno R, Levantini E, Pittet MJ, Klein AM. Single-Cell Transcriptomics of Human and Mouse Lung Cancers Reveals Conserved Myeloid Populations across Individuals and Species. *Immunity* 2019; 50: 1317-1334 e1310.

22. Boyette LB, Macedo C, Hadi K, Elinoff BD, Walters JT, Ramaswami B, Chalasani G, Taboas JM, Lakkis FG, Metes DM. Phenotype, function, and differentiation potential of human monocyte subsets. *PLoS One* 2017; 12: e0176460.

23. Crotty S. T follicular helper cell differentiation, function, and roles in disease. *Immunity* 2014; 41: 529-542.

24. Pattarini L, Trichot C, Bogiatzi S, Grandclaudon M, Meller S, Keuylian Z, Durand M, Volpe E, Madonna S, Cavani A, Chiricozzi A, Romanelli M, Hori T, Hovnanian A, Homey B, Soumelis V. TSLP-activated dendritic cells induce human T follicular helper cell differentiation through OX40-ligand. *J Exp Med* 2017; 214: 1529-1546.

25. Litsiou E, Semitekolou M, Galani IE, Morianos I, Tsoutsa A, Kara P, Rontogianni D, Bellenis I, Konstantinou M, Potaris K, Andreakos E, Sideras P, Zakynthinos S, Tsoumakidou M. CXCL13 production in B cells via Toll-like receptor/lymphotoxin receptor signaling is involved in lymphoid neogenesis in chronic obstructive pulmonary disease. *Am J Respir Crit Care Med* 2013; 187: 1194-1202.

26. Roos AB, Sanden C, Mori M, Bjermer L, Stampfli MR, Erjefalt JS. IL-17A Is Elevated in End-Stage Chronic Obstructive Pulmonary Disease and Contributes to Cigarette Smoke-induced Lymphoid Neogenesis. *Am J Respir Crit Care Med* 2015; 191: 1232-1241.

27. Cyster JG, Dang EV, Reboldi A, Yi T. 25-Hydroxycholesterols in innate and adaptive immunity. *Nat Rev Immunol* 2014; 14: 731-743.

28. Jia J, Conlon TM, Sarker RS, Tasdemir D, Smirnova NF, Srivastava B, Verleden SE, Gunes G, Wu X, Prehn C, Gao J, Heinzelmann K, Lintelmann J, Irmler M, Pfeiffer S, Schloter M, Zimmermann R, Hrabe de Angelis M, Beckers J, Adamski J, Bayram H, Eickelberg O, Yildirim AO. Cholesterol metabolism promotes B-cell positioning during immune pathogenesis of chronic obstructive pulmonary disease. *EMBO Mol Med* 2018; 10.

29. Lu E, Dang EV, McDonald JG, Cyster JG. Distinct oxysterol requirements for positioning naive and activated dendritic cells in the spleen. *Sci Immunol* 2017; 2.

30. Nish SA, Schenten D, Wunderlich FT, Pope SD, Gao Y, Hoshi N, Yu S, Yan X, Lee HK, Pasman L, Brodsky I, Yordy B, Zhao H, Bruning J, Medzhitov R. T cell-intrinsic role of IL-6 signaling in primary and memory responses. *Elife* 2014; 3: e01949.

31. Chakarov S, Fazilleau N. Monocyte-derived dendritic cells promote T follicular helper cell differentiation. *EMBO Mol Med* 2014; 6: 590-603.

32. Yamasaki S, Shimizu K, Kometani K, Sakurai M, Kawamura M, Fujii SI. In vivo dendritic cell targeting cellular vaccine induces CD4(+) Tfh cell-dependent antibody against influenza virus. *Sci Rep* 2016; 6: 35173.

33. Ryu H, Chung Y. Dyslipidemia promotes germinal center reactions via IL-27. *BMB Rep* 2018; 51: 371-372.

34. Erokhina SA, Streltsova MA, Kanevskiy LM, Telford WG, Sapozhnikov AM, Kovalenko EI. HLA-DR(+) NK cells are mostly characterized by less mature phenotype and high functional activity. *Immunol Cell Biol* 2018; 96: 212-228.

35. Lotfi-Emran S, Ward BR, Le QT, Pozez AL, Manjili MH, Woodfolk JA, Schwartz LB. Human mast cells present antigen to autologous CD4(+) T cells. *J Allergy Clin Immunol* 2018; 141: 311-321 e310.

36. Taflin C, Favier B, Baudhuin J, Savenay A, Hemon P, Bensussan A, Charron D, Glotz D, Mooney N. Human endothelial cells generate Th17 and regulatory T cells under inflammatory conditions. *Proc Natl Acad Sci U S A* 2011; 108: 2891-2896.

37. Zissel G, Ernst M, Rabe K, Papadopoulos T, Magnussen H, Schlaak M, Muller-Quernheim J. Human alveolar epithelial cells type II are capable of regulating T-cell activity. *J Investig Med* 2000; 48: 66-75.

38. Freeman CM, Martinez FJ, Han MK, Ames TM, Chensue SW, Todt JC, Arenberg DA, Meldrum CA, Getty C, McCloskey L, Curtis JL. Lung dendritic cell expression of maturation molecules increases with worsening chronic obstructive pulmonary disease. *Am J Respir Crit Care Med* 2009; 180: 1179-1188.

39. Shan M, Cheng HF, Song LZ, Roberts L, Green L, Hacken-Bitar J, Huh J, Bakaeen F, Coxson HO, Storness-Bliss C, Ramchandani M, Lee SH, Corry DB, Kheradmand F. Lung myeloid dendritic cells coordinately induce TH1 and TH17 responses in human emphysema. *Sci Transl Med* 2009; 1: 4ra10.

40. Shan M, You R, Yuan X, Frazier MV, Porter P, Seryshev A, Hong JS, Song LZ, Zhang Y, Hilsenbeck S, Whitehead L, Zarinkamar N, Perusich S, Corry DB, Kheradmand F. Agonistic induction of PPARgamma reverses cigarette smoke-induced emphysema. *J Clin Invest* 2014; 124: 1371-1381.

41. Lu W, You R, Yuan X, Yang T, Samuel EL, Marcano DC, Sikkema WK, Tour JM, Rodriguez A, Kheradmand F, Corry DB. The microRNA miR-22 inhibits the histone deacetylase HDAC4 to promote T(H)17 cell-dependent emphysema. *Nat Immunol* 2015; 16: 1185-1194.

42. You R, Lu W, Shan M, Berlin JM, Samuel EL, Marcano DC, Sun Z, Sikkema WK, Yuan X, Song L, Hendrix AY, Tour JM, Corry DB, Kheradmand F. Nanoparticulate carbon black in cigarette smoke induces DNA cleavage and Th17-mediated emphysema. *Elife* 2015; 4: e09623.

43. Tsoumakidou M, Tousa S, Semitekolou M, Panagiotou P, Panagiotou A, Morianos I, Litsiou E, Trochoutsou AI, Konstantinou M, Potaris K, Footitt J, Mallia P, Zakynthinos S, Johnston SL, Xanthou G. Tolerogenic signaling by pulmonary CD1c+ dendritic cells induces regulatory T cells in patients with chronic obstructive pulmonary disease by IL-27/IL-10/inducible costimulator ligand. *J Allergy Clin Immunol* 2014; 134: 944-954 e948.

44. Krishnaswamy JK, Gowthaman U, Zhang B, Mattsson J, Szeponik L, Liu D, Wu R, White T, Calabro S, Xu L, Collet MA, Yurieva M, Alsen S, Fogelstrand P, Walter A, Heath WR, Mueller SN, Yrlid U, Williams A, Eisenbarth SC. Migratory CD11b(+) conventional dendritic cells induce T follicular helper cell-dependent antibody responses. *Sci Immunol* 2017; 2.

45. Durand M, Walter T, Pirnay T, Naessens T, Gueguen P, Goudot C, Lameiras S, Chang Q, Talaei N, Ornatsky O, Vassilevskaia T, Baulande S, Amigorena S, Segura E. Human lymphoid organ cDC2 and macrophages play complementary roles in T follicular helper responses. *J Exp Med* 2019.

46. Jacquemin C, Schmitt N, Contin-Bordes C, Liu Y, Narayanan P, Seneschal J, Maurouard T, Dougall D, Davizon ES, Dumortier H, Douchet I, Raffray L, Richez C, Lazaro E, Duffau P, Truchetet ME, Khoryati L, Mercie P, Couzi L, Merville P, Schaeverbeke T, Viallard JF, Pellegrin JL, Moreau JF, Muller S, Zurawski S, Coffman RL, Pascual V, Ueno H, Blanco P. OX40 Ligand Contributes to Human Lupus Pathogenesis by Promoting T Follicular Helper Response. *Immunity* 2015; 42: 1159-1170.

47. Ying S, O'Connor B, Ratoff J, Meng Q, Fang C, Cousins D, Zhang G, Gu S, Gao Z, Shamji B, Edwards MJ, Lee TH, Corrigan CJ. Expression and cellular provenance of thymic stromal lymphopoietin and chemokines in patients with severe asthma and chronic obstructive pulmonary disease. *J Immunol* 2008; 181: 2790-2798.

48. Naessens T, Schepens B, Smet M, Pollard C, Van Hoecke L, De Beuckelaer A, Willart M, Lambrecht B, De Koker S, Saelens X, Grooten J. GM-CSF treatment prevents respiratory syncytial virus-

induced pulmonary exacerbation responses in postallergic mice by stimulating alveolar macrophage maturation. *J Allergy Clin Immunol* 2016; 137: 700-709 e709.

49. Morissette MC, Shen P, Thayaparan D, Stampfli MR. Disruption of pulmonary lipid homeostasis drives cigarette smoke-induced lung inflammation in mice. *Eur Respir J* 2015; 46: 1451-1460.

50. Kearley J, Silver JS, Sanden C, Liu Z, Berlin AA, White N, Mori M, Pham TH, Ward CK, Criner GJ, Marchetti N, Mustelin T, Erjefalt JS, Kolbeck R, Humbles AA. Cigarette smoke silences innate lymphoid cell function and facilitates an exacerbated type I interleukin-33-dependent response to infection. *Immunity* 2015; 42: 566-579.

51. Barnes PJ. Inflammatory mechanisms in patients with chronic obstructive pulmonary disease. *J Allergy Clin Immunol* 2016; 138: 16-27.

Figure legends

Figure 1: Human non-obstructed lungs contain a highly heterogeneous myeloid cell compartment. Myeloid cells, purified from non-obstructed human peritumoral lung tissues (n=3), were analyzed by single-cell RNA sequencing using the Seurat package. Combined single-cell transcriptomes were analyzed. (A) t-SNE representation of cell clusters identified using unsupervised clustering. Each dot represents an individual cell. Colors represent identified clusters. (B) Heatmap of scaled expression of (log values of Unique Molecular Identifiers (UMI)) for the top 20 differentially expressed genes of each cluster (based on log fold change). (C) Signature scores (arbitrary units) of individual cells for indicated gene signatures.

Figure 2: Lung cDC2 are the most potent inducers of Tfh-like cell polarization. DC subsets were purified from non-obstructed peritumoral lung tissue and co-cultured with allogeneic naïve blood $CD4^+$ T-cells. (A) Percentages of $ICOS^+PD\text{-}1^+$ T-cells in the different DC/T-cell co-cultures were determined at d7 of the co-culture via flow cytometry. Summary data graph with each symbol representing an individual donor (n=10). (B) Flow cytometry histogram of OX40 staining on $ICOS^+PD\text{-}1^+$ (purple), $ICOS^-PD\text{-}1^+$ (orange), $ICOS^+PD\text{-}1^-$ (blue) and $ICOS^-PD\text{-}1^-$ (black) T-cell subsets in cDC2/T-cell co-cultures. Representative data from 3 donors is shown. (C) Intracellular IL-21 (n=10) and CXCL13 (n=6) staining of $ICOS^+PD\text{-}1^+$ (purple), $ICOS^-PD\text{-}1^+$ (orange), $ICOS^+PD\text{-}1^-$ (blue) and $ICOS^-PD\text{-}1^-$ (black) T-cell subsets in cDC2/T-cell co-cultures after restimulation with PMA and ionomycin in the presence of Golgi-plug and Golgi-stop. Summary data graph in which each symbol represents an individual donor. (D) Percentages of $ICOS^+PD\text{-}1^+IL\text{-}21^+$ T-cells in cDC2/T-cell and cDC1/T-cell co-cultures were determined. Summary data graph in which each symbol represents an individual donor (n=10). (E) Proportions of $ICOS^+CXCR5^+$ T-cells in the different DC/T-cell co-cultures were determined at day 4. Summary data graph in which each symbol represents an individual donor

(n=6). (F) Percentages of PD-1^{hi}BCL6^{hi} cells in ICOS^{+}CXCR5^{+}, ICOS^{+}CXCR5^{-} and ICOS^{-}CXCR5^{-} T-cell subsets in the cDC2/T-cell co-cultures were determined via flow cytometry. Summary data graph in which each symbol represents an individual donor (n=6). *p<0.05, **p<0.01, ***p<0.001, Tukey's multiple comparison test (A, C, E and F) and paired student's *t*-test (D).

Figure 3: cDC2 from COPD GOLD II lungs display increased potential to promote Tfh-like cell skewing which is associated with the increased presence of Tfh-like cells in the COPD lung. (A) and (B) cDC2 were isolated from COPD GOLD II peritumoral lung tissues (n=7) and co-cultured with allogeneic naïve CD4^{+} T-cells. Proportions of ICOS^{+}PD-1^{+} T-cells (A) and ICOS^{+}PD-1^{+}IL-21^{+} T-cells (B) were determined at day 7 and compared to the respective T-cell proportions induced by cDC2 from non-obstructed peritumoral lung tissues as previously shown in Figure 2 (n=10). Shown is summary data graphs in which each symbol represents an individual donor. (C) Percentages of ICOS^{+}PD-1^{+} Tfh-like cells were determined in peritumoral lung tissue resections of COPD and non-obstructed control subjects via flow cytometry. Shown is summary data graph in which each symbol represents an individual donor (n=6 for controls and n=5 for COPD subjects). (D) Intracellular IL-21 staining of lung tissue ICOS^{+}PD-1^{+} (purple), ICOS^{-}PD-1^{+} (orange), ICOS^{+}PD-1^{-} (blue) and ICOS^{-}PD-1^{-} (black) T-cell subsets after PMA/ionomycin restimulation (+ Golgi-plug/Golgi-stop) in DC-free *in vitro* cultures. Shown are pooled data from control (full diamonds) and COPD (open diamonds) lung resections (n=11). Each symbol represents an individual donor. *p<0.05, **p<0.01, ***p<0.001, Student's *t*-test (A-C) and Tukey's multiple comparison test (D).

Figure 4: cDC2 exhibit a unique migratory pattern. (A) Surface levels of CXCR5, CXCR4 and EBI2 were measured on cDC2 and cDC1 from non-obstructed peritumoral lung resections via flow cytometry (n=7 for CXCR5, n=5 for CXCR4 and n=7 for EBI2). Summary data graphs (mean MFI corrected for background intensity) for the indicated markers are shown. Each

symbol represents an individual donor. (B) Surface EBI2 levels on $ICOS^{+}PD\text{-}1^{+}$ (purple), $ICOS^{-}PD\text{-}1^{+}$ (orange), $ICOS^{+}PD\text{-}1^{-}$ (blue) and $ICOS^{-}PD\text{-}1^{-}$ (black) T-cell subsets in the lung measured via flow cytometry. Summary data graph (mean MFI corrected for background intensity) of pooled control (full diamonds) and COPD (open diamonds) lung samples (n=10). Each symbol represents an individual donor. (C) Correlations of whole lung *EBI2*, *CH25H*, *CYP1B1* and *CYP7B1* mRNA expression with COPD disease severity (GOLD stage and %FEV1) and whole lung *CXCL13* mRNA as a marker for TLO formation. (D) Correlation of whole lung *CH25H* mRNA expression with whole lung *EBI2* mRNA expression. Data in C and D are derived from a publicly available GSE-set (GSE47460). Healthy control subjects n=116; GOLD I n=24; GOLD II n=97; GOLD III n=32 and GOLD IV n=54. (E) *In situ* visualization of *CH25H* mRNA (brown) in COPD GOLD IV explanted lung tissue TLOs via RNAscope duplex technology (n=5). *CD19* mRNA (red) is used to delineate the B-cell follicle of the TLO. *p<0.05, **p<0.01, ***p<0.001, (A) Student's *t*-test, (B) Tukey's multiple comparison test (C) and Holm-Sidak's multiple test correction was used. To test for correlation of expression for the indicated genes within all study subjects, linear regression analysis and Pearson's correlation test were used to calculate the correlation coefficient r, R2 and p-value of correlation.

Figure 5: cDC2 reside in the follicular T-cell zone of established COPD GOLD IV TLO. Representative confocal fluorescence images of TLOs located in COPD GOLD IV explanted lungs (n=5). CD19 (blue) (AF594) and CD3ε (purple) (AF647) was used to define the B- and T-cell zone of the TLO respectively. CD11c (green) (FITC) and CD1c (red) (AF542) were used to identify cDC2 (white arrows). Hoechst was used as nuclear counter staining (grey). Scale bars 100μm.

Figure 6: cDC2 express increased levels of OX40L and transcriptional signatures related to Tfh-cell priming. Surface levels of ICOSL, PD-L1 and OX40L were measured on cDC2

and cDC1 from (A) non-obstructed and (B) COPD GOLDII (OX40L) peritumoral lung tissue via flow cytometry. Summary data graphs of the indicated co-stimulatory markers are depicted in A and representative flow cytometry histograms and summary data graph for OX40L is shown in B. Each symbol represents an individual donor (n=5 for ICOSL, n=6 for PD-L1, n=7 for control OX40L control and n=5 for COPD OX40L). *p<0.05, **p<0.01, Student's *t*-test. (C) cDC2 were isolated from non-obstructed peritumoral lung resections (n=3) and co-cultured with allogeneic naïve $CD4^+$ T-cells in the presence of an OX40L blocking antibody (oxelumab) or an IgG isotype control. Proportions of $ICOS^+PD\text{-}1^+$ T-cells were determined at day 7. Shown is the combined data graph in which each symbol represents an individual donor. (D) and (E) cDC2 and cDC1 were FACS-sorted from non-obstructed peritumoral lung resections (n=5) and the RNA transcriptomic profile of these subsets was generated via NGS. (D) Canonical pathways significantly (signif) upregulated (red) and downregulated (blue) (Fisher's exact test, $-\log_{10} P$ values for each represented pathway are shown) in transcriptional signatures in cDC2 vs cDC1 as predicted by Ingenuity Pathway Analysis (IPA). (E) Significant putative regulators with predicted activating (red) or inhibitory (blue) influence on transcriptional signatures in cDC2 vs cDC1 from non-obstructed lungs, as determined by IPA.

Figure 7: cDC2 drive lymphoid neogenesis during COPD; a working model. Elevated pulmonary levels of CXCL12, CXCL13 and cholesterol metabolites, produced during COPD, attract cDC2 and $CD4^+$ T-cells to the site of TLO formation. Upon encounter, cDC2 drive IL-21^+ Tfh-like cell polarization via the OX40L-OX40 axis and the secretion of cytokines like IL-6, IL-1β and TGF-β. The chronicity of this self-amplifying loop results in the formation of well-established TLOs during late-stage COPD in which Tfh-like cell clonality and proliferation is further sustained by cDC2.

Tables

Table 1: Summary of subject demographics, smoking history, and spirometry

Group	Control	COPD GOLD II	COPD GOLD IV
Subjects, *n*	35	7	5
Sex: M,F	14, 21	3, 4	0, 5
Age, yr	65 (10)	70 (6)	61 (8)
Smoking, pack-years (active and former)	28 (12)	41 (10)	45 (9)
Smoking status: never, active, former	8, 1, 26	0, 0, 7	0, 0, 5
FEV_1, % pred	94 (17)	57 (7)	27 (17)
DL_{CO}, % pred	74 (14)	63 (10)	31 (4)

Definition of abbreviations: % pred = percentage of the predicted value; COPD = Chronic Obstructive Pulmonary Disease

Data are represented as mean (SD)

Figure 1

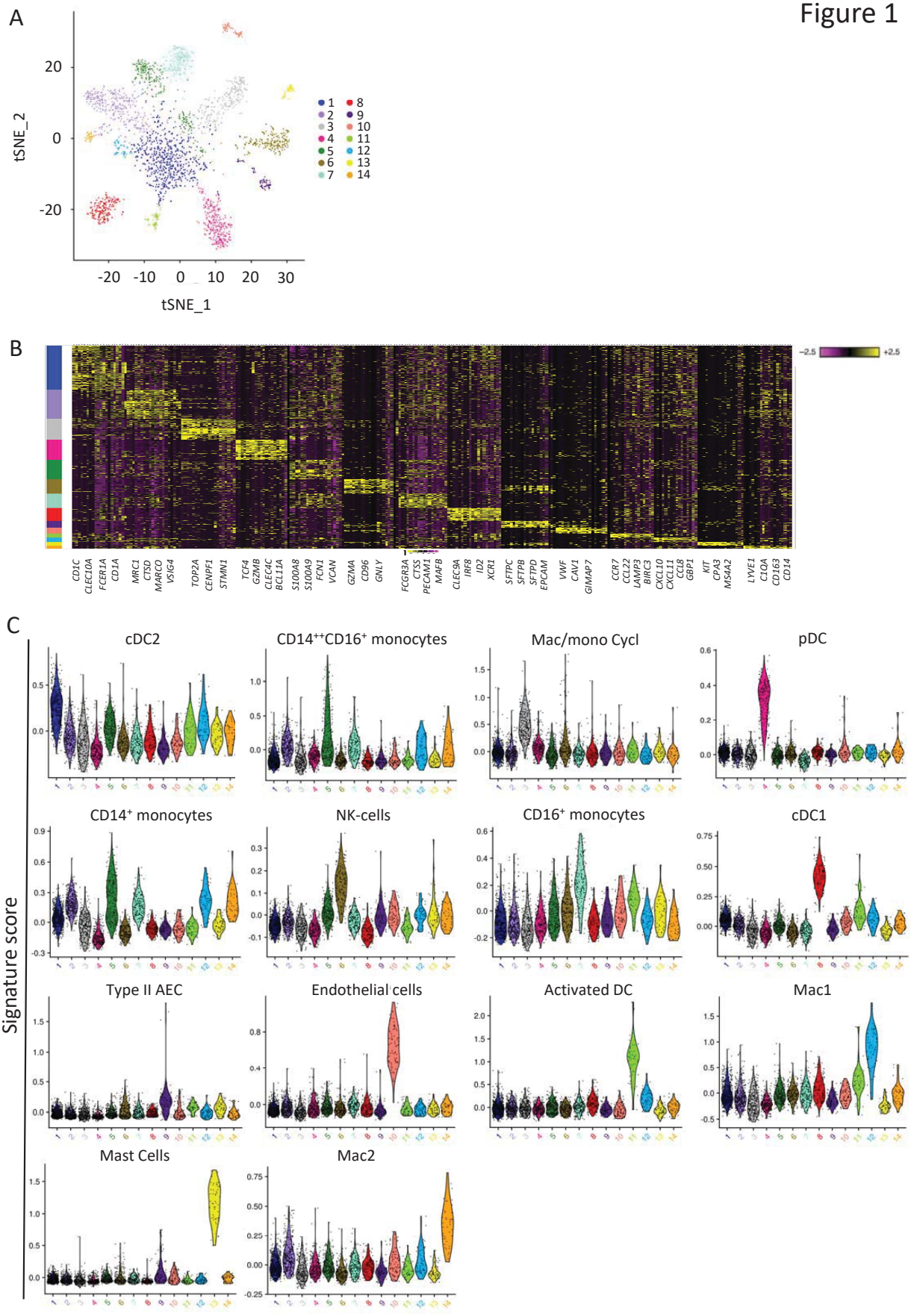
A
tSNE_2
tSNE_1
20
0
-20
-20 -10 0 10 20 30
1 2 3 4 5 6 7 8 9 10 11 12 13 14
B
−2.5 +2.5
CD1C CLEC10A FCER1A CD1A MRC1 CTSD MARCO VSIG4 TOP2A CENPF1 STMN1 TCF4 GZMB CLEC4C BCL11A S100A8 S100A9 FCN1 VCAN GZMA CD96 GNLY FCGR3A CTSS PECAM1 MAFB CLEC9A IRF8 ID2 XCR1 SFTPC SFTPB SFTPD EPCAM VWF CAV1 GIMAP7 CCR7 CCL22 LAMP3 BIRC3 CXCL10 CXCL11 CCL8 GBP1 KIT CPA3 MS4A2 LYVE1 C1QA CD163 CD14
C
Signature score
cDC2
CD14++CD16+ monocytes
Mac/mono Cycl
pDC
CD14+ monocytes
NK-cells
CD16+ monocytes
cDC1
Type II AEC
Endothelial cells
Activated DC
Mac1
Mast Cells
Mac2

Figure 2

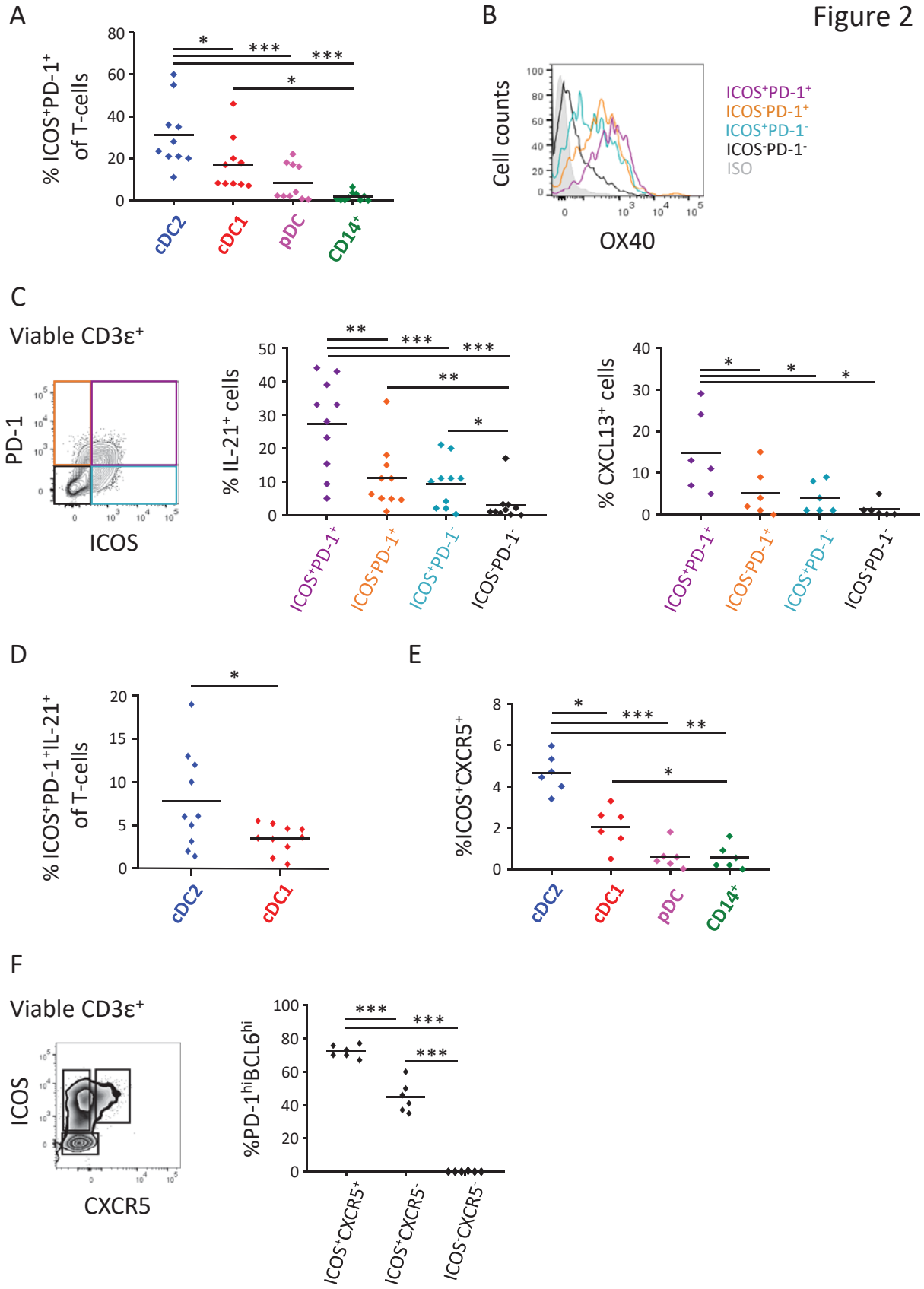
A
% ICOS+PD-1+ of T-cells
cDC2
cDC1
pDC
CD14+
B
Cell counts
OX40
ICOS+PD-1+
ICOS-PD-1+
ICOS+PD-1-
ICOS-PD-1-
ISO
C
Viable CD3ε+
PD-1
ICOS
% IL-21+ cells
% CXCL13+ cells
D
% ICOS+PD-1+IL-21+ of T-cells
E
%ICOS+CXCR5+
F
Viable CD3ε+
ICOS
CXCR5
%PD-1hiBCL6hi

Figure 3

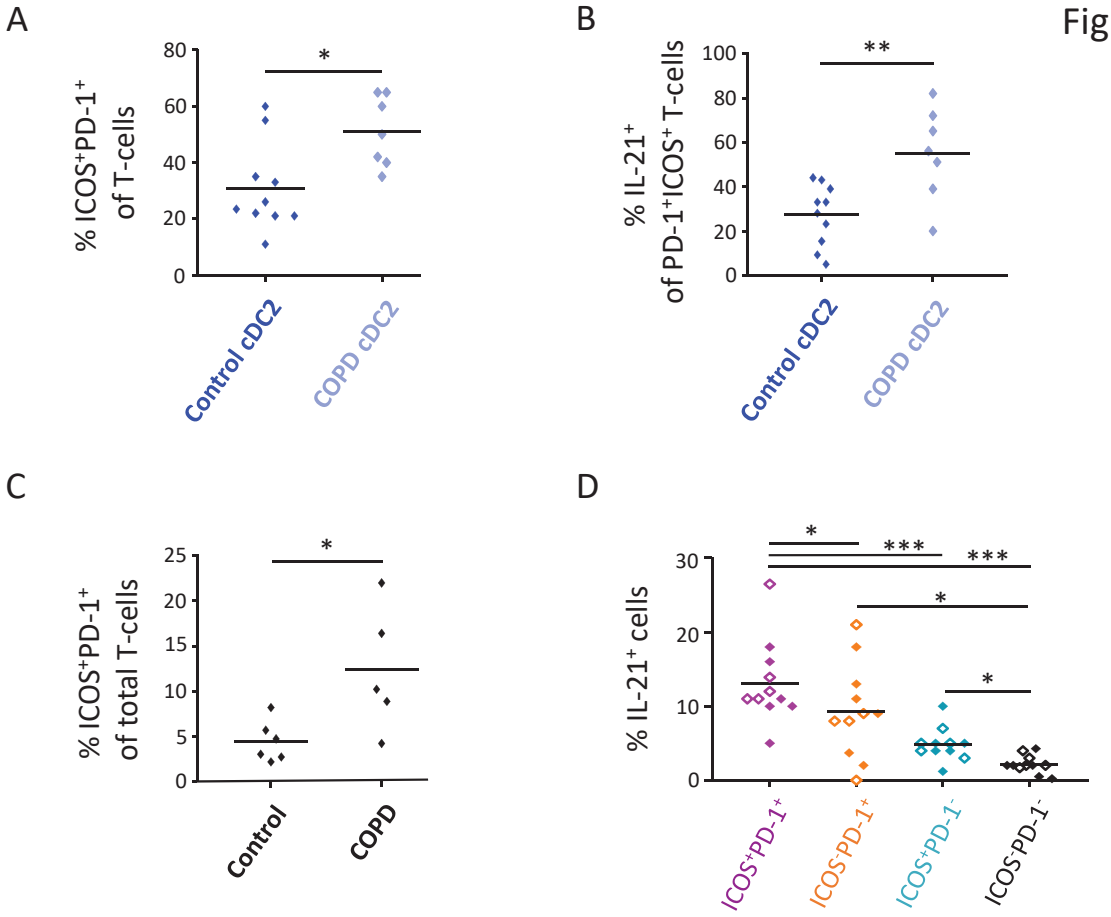
A
% ICOS+PD-1+ of T-cells
80
60
40
20
0
*
Control cDC2
COPD cDC2
B
% IL-21+ of PD-1+ICOS+ T-cells
100
80
60
40
20
0
**
Control cDC2
COPD cDC2
C
% ICOS+PD-1+ of total T-cells
25
20
15
10
5
0
*
Control
COPD
D
% IL-21+ cells
30
20
10
0
*
***
***
*
*
ICOS+PD-1+
ICOS-PD-1+
ICOS+PD-1-
ICOS-PD-1-

Figure 4

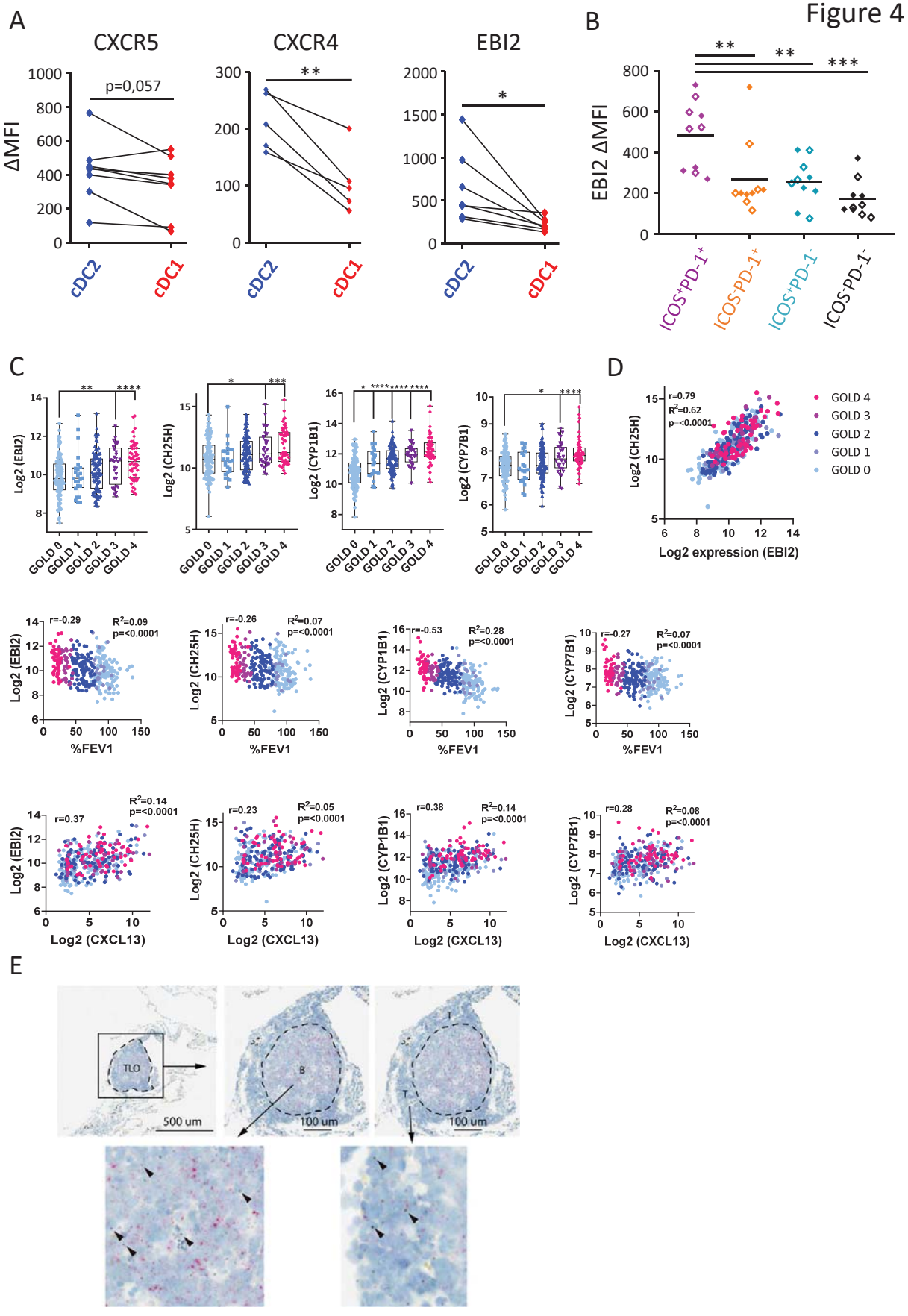
A
CXCR5
CXCR4
EBI2
ΔMFI
p=0,057
**
*
cDC2
cDC1
B
EBI2 ΔMFI
**
**
***
ICOS+PD-1+
ICOS-PD-1+
ICOS+PD-1-
ICOS-PD-1-
C
Log2 (EBI2)
Log2 (CH25H)
Log2 (CYP1B1)
Log2 (CYP7B1)
GOLD 0
GOLD 1
GOLD 2
GOLD 3
GOLD 4
D
r=0.79
R2=0.62
p=<0.0001
Log2 expression (EBI2)
GOLD 4
GOLD 3
GOLD 2
GOLD 1
GOLD 0
r=-0.29
R2=0.09
p=<0.0001
r=-0.26
R2=0.07
p=<0.0001
r=-0.53
R2=0.28
p=<0.0001
r=-0.27
R2=0.07
p=<0.0001
%FEV1
r=0.37
R2=0.14
p=<0.0001
r=0.23
R2=0.05
p=<0.0001
r=0.38
R2=0.14
p=<0.0001
r=0.28
R2=0.08
p=<0.0001
Log2 (CXCL13)
E
TLO
B
T
500 um
100 um
100 um

Figure 5

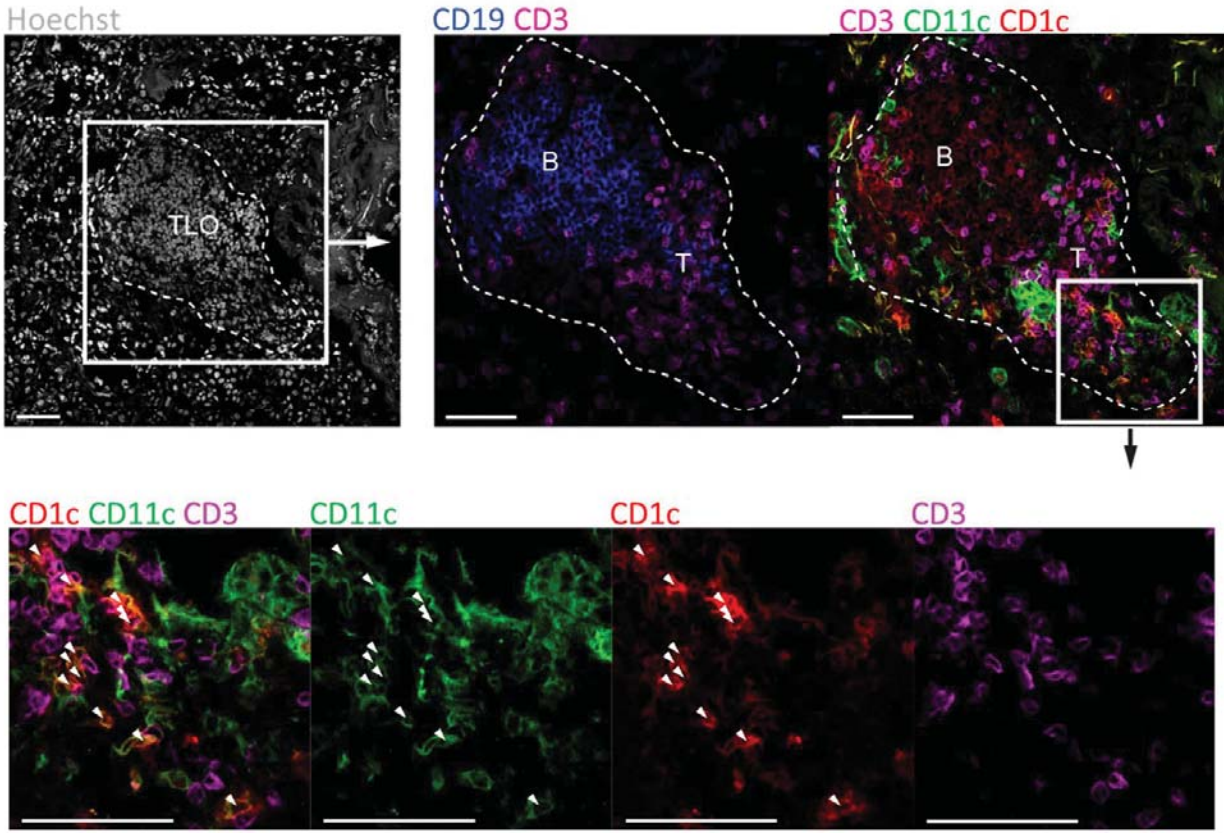
Hoechst
TLO
CD19 CD3
B
T
CD3 CD11c CD1c
B
T
CD1c CD11c CD3
CD11c
CD1c
CD3

Figure 6

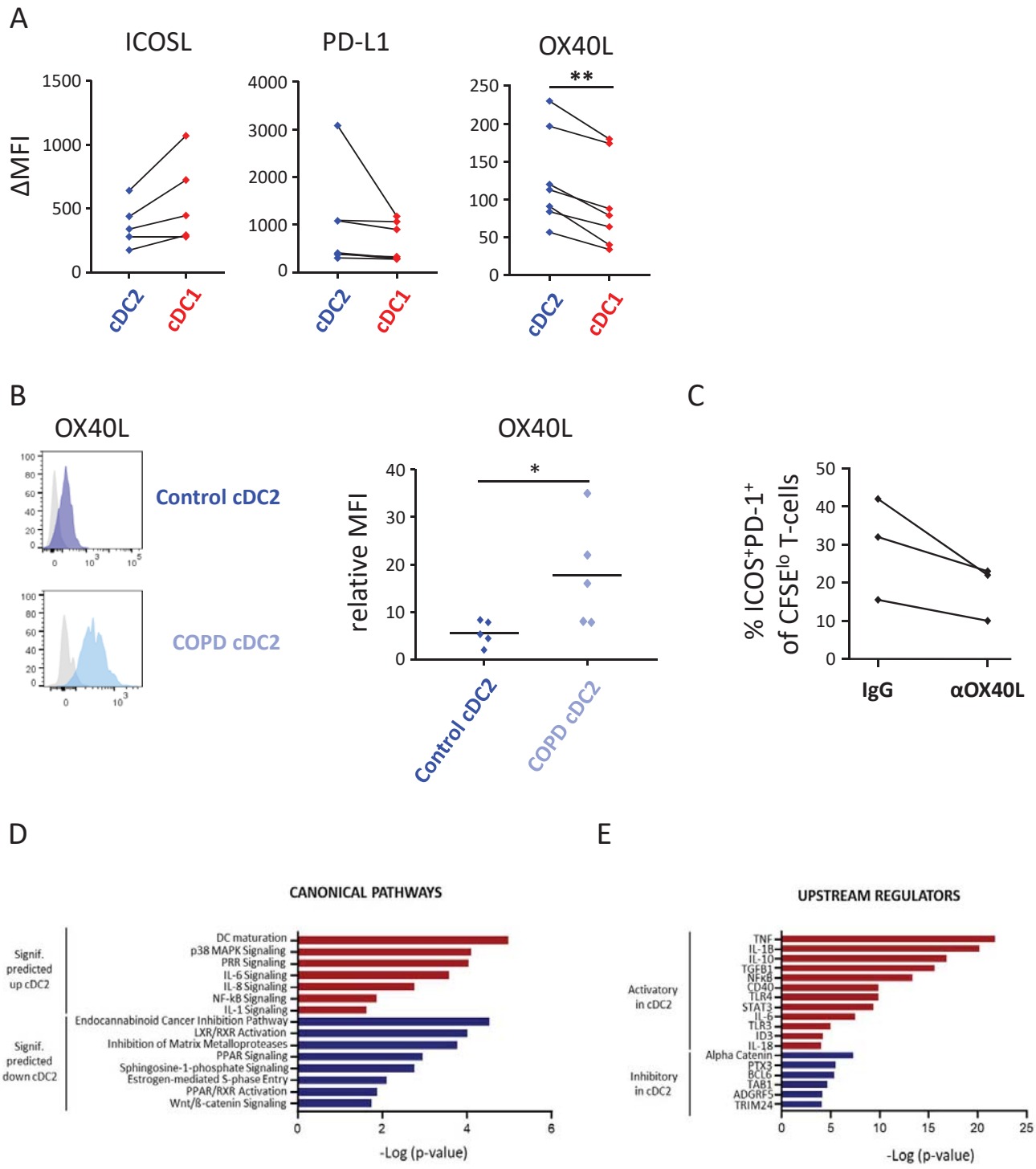
A
ICOSL
PD-L1
OX40L
ΔMFI
1500
1000
500
0
4000
3000
2000
1000
0
250
200
150
100
50
0
**
cDC2
cDC1
B
OX40L
Control cDC2
COPD cDC2
OX40L
relative MFI
40
30
20
10
0
*
Control cDC2
COPD cDC2
C
% ICOS+PD-1+ of CFSElo T-cells
50
40
30
20
10
0
IgG
αOX40L
D
CANONICAL PATHWAYS
Signif. predicted up cDC2
Signif. predicted down cDC2
DC maturation
p38 MAPK Signaling
PRR Signaling
IL-6 Signaling
IL-8 Signaling
NF-kB Signaling
IL-1 Signaling
Endocannabinoid Cancer Inhibition Pathway
LXR/RXR Activation
Inhibition of Matrix Metalloproteases
PPAR Signaling
Sphingosine-1-phosphate Signaling
Estrogen-mediated S-phase Entry
PPAR/RXR Activation
Wnt/ß-catenin Signaling
0
2
4
6
-Log (p-value)
E
UPSTREAM REGULATORS
Activatory in cDC2
Inhibitory in cDC2
TNF
IL-1B
IL-10
TGFB1
NFkB
CD40
TLR4
STAT3
IL-6
TLR3
ID3
IL-18
Alpha Catenin
PTX3
BCL6
TAB1
ADGRF5
TRIM24
0
5
10
15
20
25
-Log (p-value)

Figure 7

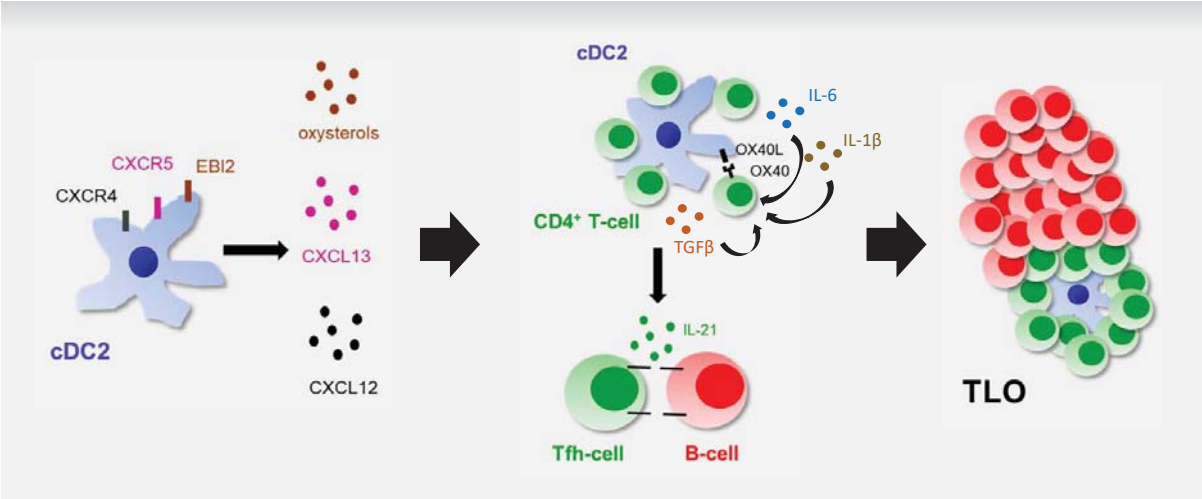
oxysterols
CXCR5
EBI2
CXCR4
CXCL13
cDC2
CXCL12
cDC2
IL-6
IL-1β
OX40L
OX40
CD4⁺ T-cell
TGFβ
IL-21
Tfh-cell
B-cell
TLO

Supplemental methods and results

Human Lung Conventional Dendritic Cells Orchestrate Lymphoid Neogenesis During COPD

Thomas Naessens, Yannick Morias[*], Eva Hamrud[*], Ulf Gehrmann, Ramachandramouli Budida, Johan Mattsson, Tina Baker, Gabriel Skogberg, Elisabeth Israelsson, Kristofer Thörn, Martijn J. Schuijs, Bastian Angermann, Faye Melville, Karl J Staples, Danen M Cunoosamy[#] and Bart N Lambrecht[#]

*Authors contributed equally to this paper

#Authors co-supervised the study

Supplemental Methods

Human lung samples

Lung samples were obtained from 35 non-obstructed control subjects (i.e. normal lung function, among whom 8 never-smokers, 1 current smoker and 26 former smokers) and 12 patients with COPD undergoing lung surgery, either for resection of a solitary tumor (24 control subjects and 7 COPD GOLD II subjects) or transplantation for very severe COPD (5 COPD GOLD IV subjects) at the Sahlgrenska University Hospital, Gothenburg, Sweden. All subjects underwent preoperative post-bronchodilator spirometry. Subjects were categorized by based on the 2001 classification of the Global Initiative for Chronic Obstructive Lung Disease (GOLD) (1). In case of resected tissue, macroscopically healthy lung was sampled. We defined ex-smokers as having quit smoking habits for at least 6 months before surgery.

Human lung sample processing

Lung tissue was extensively flushed with PBS (Invitrogen) to remove excessive blood contamination and alveolar cells. The flushed tissue was subsequently cut into small pieces (0,5 cm x 0,5 cm) and incubated in a digestion buffer, containing 1mg/ml Collagenase D (Sigma-Aldrich) in RPMI medium (Invitrogen), for 30 minutes at 37°C. Afterwards, the lung tissue pieces were minced over a 100 μm cell strainer (Miltenyi Biotec) to obtain a single cell suspension.

Single-cell RNA sequencing of human lung myeloid cells

FACS-sorted myeloid subpopulations were stained with Hoechst 33342 and Propidium Iodide dye mix (Invitrogen, MA, USA) and diluted to 20,000 cells/mL. The cells were dispensed into nanowells using the ICELL8 Single-Cell System (Takara Bio, Japan), and single live cells were identified using CellSelect software (WaferGen, CA, USA). After a

freeze-thaw cycle, the cells were processed for RT-PCR and cDNA amplification according to the manufacturer's instructions. The cDNA amplicons were then pooled and concentrated using Zymo DNA Clean & Concentrator^{TM}-5 kit (Zymo Research, CA, USA) followed by cDNA purification using 0.6X AMPure XP beads (Beckman Coulter, IN, USA) and quantification using Qubit dsDNA HS Assay Kit on the Qubit fluorometer (Thermo Fisher, MA, USA). The cDNA was quality checked using HS NGS kit on a Fragment Analyzer (Agilent, CA, USA). The purified cDNA was subsequently used for Nextera XT (Illumina, CA, USA) library preparation and amplification. A total of three lung tissues were processed individually for the library preparation. The quality and quantity of the libraries was analyzed using HS NGS Fragment Analyzer and Qubit dsDNA HS Assay Kit respectively. Sample libraries were pooled in equimolar concentrations and diluted and denatured according to Illumina guidelines. Sequencing was performed using a High Output 150 cycle kit on an Illumina NextSeq550 using 26 cycles for read1, and 126 cycles for read2.

Raw sequence processing and quality control. RNA-seq fastq files were processed using bcbio-nextgen (version 1.1.0) (bcbio-nextgen. Validated, scalable, community developed variant calling, RNA-seq and small RNA analysis. Available from: https://github.com/chapmanb/bcbio-nextgen) where reads were mapped to the human genome build hg38 (GRCh38.92 version 25) using hisat2 (version 2.1.0) (2). For the bulk dataset this yielded between 37.2 – 64.9 M mapped reads per sample (with a mean of 49.4 M). No filtering of samples or genes was performed on the bulk RNA sequencing data. For the single cell dataset, 180 M reads aligned to genes. Gene level quantifications, counts and transcript per million (TPM), were generated with featurecounts (version 1.4.4) (3) and sailfish (version 0.10.1) (4), respectively, all within bcbio. The single cell dataset was additionally demultiplexed using UMIs with the umis (version 1.0.0), also within the bcbio framework.

Quality control included filtering by, the number of genes per cell, mitochondrial gene contribution and minimum gene representation across cells.

Single cell sequencing data clustering and cluster identification. For the single cell data, most analyses were performed using Seurat toolkit (4) (https://satijalab.org/seurat/, version 3.1.0) available in R (R version 3.5.1). Single cell data was processed to regress out unwanted sources of variation. Cells from the three donors were aggregated into separate Seurat objects, these were then aligned to each other using canonical correlation analysis. Clustering was conducted using a graph-based clustering approach within the framework of Seurat. 14 clusters that were found were used for all subsequent analysis and visualized using the Seurat function TSNEplot. All plots were made using R (version 3.5.2, www.r-project.org) and Seurat (version 3.1.0). Unique marker genes per cluster were extracted with the Seurat function FindAllMarkers and the top 20 genes which displayed the highest log fold change in expression between clusters were extracted. A phylogenetic tree relating to the 'average' cell from each identity class was constructed from the dataset using the Seurat function BuildClusterTree and the resulting scaled expression data for the top 20 genes per cluster were plotted using the Seurat function DoHeatmap. To confirm cluster identities, published gene signatures for blood DC subtypes from Villani *et al.* (5) and Zilionis *et al.* (6) were matched against our clusters. The gene lists from Villani *et al.* were first filtered to remove any blood-specific genes that did not appear in any of our single cell dataset. A signature score was then calculated for each signature and cluster using the Seurat function *AddModuleScore*. Resulting scores were plotted using the Seurat function *VlnPlot*.

Next Generation RNA transcriptome Sequencing of human lung DC subsets

Total RNA preparation. Sorted lung DC subsets were resuspended in 350 µl of RLT Plus buffer (Qiagen) and stored at −80° C. Cell lysates were thawed, and total RNA was

extracted using RNeasy Plus Micro Kit (Qiagen) according to the manufacturer's protocol. RNA quality and quantity were assessed on the Fragment Analyzer platform (AATI) using high sensitivity RNA analysis kit. Only samples with RNA Integrity Number >8 were subsequently used.

Whole transcriptome profiling by RNA sequencing. 1.5 ng of total RNA was used as input to create total RNA libraries using Ovation® SoLo RNA-Seq System (NuGEN Technologies) according to the manufacturer's protocol. Libraries were validated on the Fragment Analyzer platform (AATI) using standard sensitivity NGS fragment analysis kit and the concentration was determined using Quant-iT dsDNA High Sensitivity assay kit on the Qubit fluorometer (Thermo Fisher). Sample libraries were pooled in equimolar concentrations, diluted, and denatured according to Illumina guidelines. Sequencing was performed using a High Output Kit v2 (150 cycles) on an Illumina NextSeq500.

Data analysis. The TPM (transcript per million) counts from the bulk RNA sequencing dataset of the FACs-sorted cDC1, cDC2, pDC and $CD14^+$ monocytes were log transformed and expression of genes of interest were plotted as a heatmap using the function *pheatmap* (7) (pheatmap: Pretty Heatmaps, version 0.12, https://CRAN.R-project.org/package=pheatmap). Ingenuity Pathway Analysis (IPA; QIAGEN) was used to functionally categorize differentially expressed genes and to biocomputationally identify putative upstream regulators responsible for differential gene expression signatures.

Flow cytometry

Extracellular surface marker staining. Lung single cell suspensions were incubated with Aqua LIVE/DEAD (Thermofisher) in PBS for 15 minutes at 4°C. After 2 washing steps with PBS, cells were stained in PBS containing 0,5% Fetal Calf Serum (FCS) (Invitrogen) and 2mM EDTA (Invitrogen) with anti-human CD45-BV605 (clone HI30), HLA-

DR-BV786 (clone G46-6), CD3ε-FITC (clone UCHT1), CD19-FITC (clone HIB19), CD56-FITC (clone B159), CD66b-FITC (clone G10F5), CD16-PerCP-Cy5.5 (clone 3G8), CD11c-PE-CF594 (clone B-ly6), CD141-BV711 (clone 1A4), CD3ε-PE-CF594 (clone UCHT1), ICOS-BV421 (clone DX29), CXCR5-PerCP-Cy5.5 (clone RF8B2), CXCR5-BUV395 (clone RF8B2), CXCR4-BUV395 (clone 12G5), PD-L1-BUV395 (clone MIH1), FcεRI-PE (clone AER37) (all from BD Biosciences), CD123-PE-Cy7 (clone 6H6), CD172a-APC (clone 15-414), CD14-AF700 (clone 63D3), CD1c-BV421 (L161), CLEC9a-APC (clone 8F9), XCR1-PE (clone S15046E), CD206-APC (clone 15-2), CD1a-PE-Cy7 (clone HI149), PD-1-BV711 (clone EH12.2H7), OX40-PE-Cy7 (clone Ber-ACT35), EBI2-PE (clone SA313E4), ICOSL-PE-Cy7 (clone 2D3), CD1a-PE-Cy7 (clone HI149) (all from Biolegend) and OX40L-PE (clone ANC10G1) (Ancell) for 30 minutes at 4°C.

Intracellular cytokine staining. To assess the expression of intracellular cytokines, cells were stimulated with PMA (30ng/ml) and ionomycin (1µg/ml) (both from Sigma) for 6h in the presence of GolgiPlug and GolgiStop (both from BD Biosciences) for the last 4h. After stimulation, extracellular surface markers were stained before cells were fixed and permeabilized (Fixation/Permeabilization Buffer Set, BD Biosciences). Next, cells were stained with anti-human IL-21-eFluor660 (clone 3A3-N2) (eBioscience), CXCL13-PE (clone 53610) (R&D Systems) and IFN-γ-AF700 (clone B27) (BD Biosciences) for 30 minutes at 4°C in Perm/Wash buffer (BD Biosciences).

Intracellular transcription factor staining. To assess the expression of intracellular transcription factors, cells were stained for extracellular markers before fixation and permeabilization (Fixation/Permeabilization Buffer Set, eBioscience). Next, cells were stained with anti-human unconjugated Bcl6 (rabbit polyclonal) (Abcam), IRF4-PE-Cy7 (clone 3E4) and IRF8-APC (clone V3GYWCH) (both from eBioscience) for 30 minutes at 4°C in Permeabilization Buffer (eBioscience). To detect the rabbit Bcl6, samples were incubated with

goat anti-rabbit IgG-PE (Invitrogen) for 15 minutes at 4°C in Permeabilization Buffer (eBioscience).

All samples were acquired on a FACS Fortessa instrument (BD Biosciences) and data was analyzed via FlowJo (Treestar).

Lung DC subset FACS sorting

The HLA-DR$^+$ cell fraction was prepurified from total lung cells via the MACS HLA-DR$^+$ purification kit according to manufacturer's protocol (Miltenyi Biotec). HLA-DR$^+$ cells were stained with Aqua LIVE/DEAD, anti-human CD45, HLA-DR, Lineage (CD3ε, CD19, CD56, CD66b), CD11c, CD16, CD141, CD172a, CD1c, CD14 as previously described in this online methods section. Subsequently, DC subsets were sorted with a FACS Aria III instrument (BD Biosciences).

Blood naïve CD4$^+$ T cell isolation and CFSE labeling

Peripheral blood was collected from healthy subjects via venous puncture in Gothenburg, Sweden, under written informed consent. The study was reviewed and approved by the ethical committee/review board in Gothenburg, Sweden, according to the Declaration of Helsinki (number 033-10). Peripheral Blood Mononuclear Cells (PBMC) were prepared by blood centrifugation on a Ficoll gradient (Lymphoprep, Greiner Bio-One). PBMCs were viability frozen in Fetal Calf Serum (FCS) with 10% dimethyl sulfoxide (DMSO) (both Invitrogen) until lung tissue was obtained from the Sahlgrenska Hospital (Gothenburg, Sweden). Naïve CD4$^+$ T cells were isolated from thawed PBMC aliquots by negative selection using the Human Naïve CD4$^+$ T Cell Isolation Kit according to the manufacturer's instructions (Miltenyi Biotec). After isolation, cells were stained with 0,25μM CarboxyFluorescein Succinimidyl Ester (CFSE) (eBioscience) for 10 minutes at room temperature in PBS

(Invitrogen). $CD4^+$ T-cell purity and viability were assessed before each experiment via flow cytometry.

Mixed Leukocyte Reaction (MLR)

Sorted lung DC (5000) were co-cultured with purified CFSE-labeled allogeneic naïve blood $CD4^+$ T-cells (25000) in RPMI medium supplemented with Penicillin/Streptomycin, L-Glutamine and 10% heat-inactivated FCS (all from Invitrogen). After 4 days or 6-7 days, intracellular Bcl6 expression and intracellular IL-21, CXCL13 and IFN-γ levels respectively, were analyzed via flow cytometry as previously described in this online methods section. In some experiments, 1µg/ml anti-human OX40L (oxelumab) or IgG isotype control (both from Biovision) was added.

RNAscope of GOLD IV COPD lung TLO

Lung tissue biopsies were collected, fixed in formalin, dehydrated and embedded in paraffin according to standard protocol. Blocks were cut into 4 µm sections and placed on superfrost plus glasses (ThermoFischer scientific). RNAscope 2.5 LS Duplex *in situ* hybridization was performed according to manufacturer´s protocol (Advanced Cell Diagnostics, Newark, CA) on a Leica Bond Rx autostainer (Leica). Heat induced epitope retrieval was performed for 15 minutes at 95°C using ER2 and protease was applied for 15 minutes. Probes used were: Hs-CD19 and Hs-CH25H. Chromogens applied were bond polymer define detection (brown) and bond polymer refine red detection (both Leica Biosystems) and sections were counterstained with hematoxylin. Slides were mounted using pertex mounting medium and scanned on an aperio scan scope at 20x magnification.

Fluorescence imaging of GOLD IV COPD lung TLO

Lung tissue biopsies were collected and embedded in OCT. Blocks were cut into 4 µm sections and placed on superfrost plus glasses (ThermoFischer scientific). Samples were

fixed in aceton (Sigma-Aldrich) for 15 minutes at room temperature. Subsequently, samples were blocked with IHC/ICC Blocking Buffer (eBioscience) for 15 minutes at room temperature. Afterwards, samples were stained with CD3ε-AF647 (clone UCHT1), CD11c-FITC (clone B-ly6) (both BD Biosciences), CD19-Biotin/AF594 (clone HIB19), CD1c-Biotin/AF542 (clone L161) (both Biolegend) and Hoechst nuclear staining (Thermofisher Scientific). Biotin pre-labeling with fluorochromes was performed using the Flexistain™ labeling kit according to the manufacturer's protocol (Kromnigon AB, Sweden). Microscopy images were acquired using an LSM 880 system (Carl Zeiss Microscopy, Germany) equipped with a Zeiss Image Z.1 microscope, Plan-Apochromat 40x/1,3 objective (Carl Zeiss Microscopy, Germany). Brightness and contrast were adjusted using the Zen software (Black ed. v. 2,3, Carl Zeiss Microscopy, Germany).

Statistics

Statistical analyses were calculated with GraphPad Prism (version 8) (GraphPad Software Inc, US) and the tests used are mentioned in the figure legends. *P* values less than 0,05 were considered as significant.

References

1. Pauwels RA, Buist AS, Calverley PM, Jenkins CR, Hurd SS, Committee GS. Global strategy for the diagnosis, management, and prevention of chronic obstructive pulmonary disease. NHLBI/WHO Global Initiative for Chronic Obstructive Lung Disease (GOLD) Workshop summary. *Am J Respir Crit Care Med* 2001; 163: 1256-1276.

2. Kim D, Langmead B, Salzberg SL. HISAT: a fast spliced aligner with low memory requirements. *Nat Methods* 2015; 12: 357-360.

3. Liao Y, Smyth GK, Shi W. featureCounts: an efficient general purpose program for assigning sequence reads to genomic features. *Bioinformatics* 2014; 30: 923-930.

4. Patro R, Mount SM, Kingsford C. Sailfish enables alignment-free isoform quantification from RNA-seq reads using lightweight algorithms. *Nat Biotechnol* 2014; 32: 462-464.

5. Villani AC, Satija R, Reynolds G, Sarkizova S, Shekhar K, Fletcher J, Griesbeck M, Butler A, Zheng S, Lazo S, Jardine L, Dixon D, Stephenson E, Nilsson E, Grundberg I, McDonald D, Filby A, Li W, De Jager PL, Rozenblatt-Rosen O, Lane AA, Haniffa M, Regev A, Hacohen N. Single-cell RNA-seq reveals new types of human blood dendritic cells, monocytes, and progenitors. *Science* 2017; 356.

6. Zilionis R, Engblom C, Pfirschke C, Savova V, Zemmour D, Saatcioglu HD, Krishnan I, Maroni G, Meyerovitz CV, Kerwin CM, Choi S, Richards WG, De Rienzo A, Tenen DG, Bueno R, Levantini E, Pittet MJ, Klein AM. Single-Cell Transcriptomics of Human and Mouse Lung Cancers Reveals Conserved Myeloid Populations across Individuals and Species. *Immunity* 2019; 50: 1317-1334 e1310.

7. Kolde R, Vilo J. GOsummaries: an R Package for Visual Functional Annotation of Experimental Data. *F1000Res* 2015; 4: 574.

Supplemental figure legends

Figure E1: Human non-obstructed lungs contain a highly heterogeneous myeloid cell compartment. (A) Gating strategy for isolating different $Lin^-HLA\text{-}DR^+$ subsets from non-obstructed peritumoral lung resections. Representative flow cytometry plots showing identification of the different DC subsets in human non-obstructed peritumoral lung tissue. Within the viable $CD45^+Lin^-HLA\text{-}DR^+$ cell gate, pDC were identified as $CD11c^-CD123^+$. cDC1 were $CD16^-CD11c^+CD172a^-CD141^+$ while cDC2 were $CD16^-CD11c^+CD172a^+CD1c^+$. Furthermore, $CD14^+$ monocytes were $CD16^-CD11c^+CD172a^+CD1c^-CD14^+$ and $CD16^+$ monocytes were gated as $CD16^+CD11c^+$ cells containing both $CD16^+CD14^-$ and $CD16^+CD14^+$ fractions. Finally, a $Lin^-HLA\text{-}DR^+$ population was found that scored negative for all markers included in the flow cytometry panel. This population was considered as unidentified (un). Shown are representative dot plots from 3 donors (B) *t*-SNE feature plots of the indicated genes defining expression levels in the different clusters. Each dot represents an individual cell (n=3 donors). (C) Flow cytomtery analysis of the different DC subsets from non-obstructed peritumoral lung resections revealed a $CD14^+$ cDC2 fraction and heterogeneous FcεRI and CD1a expression within cDC2. Shown are representative histograms from 3 donors. (D) Flow cytometry plots depicting expression of FcεRI, CD1a, IRF8 and IRF4 by $CD1c^+CD14^-$ and $CD1c^+CD14^+$ cDC2. Shown are representative plots of 3 non-obstructed peritumoral lung resections.

Figure E2: Lung cDC2 are the most potent inducers of Tfh-like cell polarization. DC subsets were purified from non-obstructed peritumoral lung resections and co-cultured with allogeneic naïve blood $CD4^+$ T-cells that were prelabeled with CFSE. (A) Percentages of $ICOS^+PD\text{-}1^+$ T-cells (n=10) in the different DC/T-cell co-cultures were determined at d7 of the co-culture via flow cytometry. Shown are representative flow cytometry plots for the different DC/T-cell co-cultures corresponding to the cumulative data depicted in Figure 2A. (B)

Intracellular IL-21 (n=10) and CXCL13 (n=6) staining of $ICOS^+PD\text{-}1^+$ (purple), $ICOS^-PD\text{-}1^+$ (orange), $ICOS^+PD\text{-}1^-$ (blue) and $ICOS^-PD\text{-}1^-$ (black) T-cell subsets in cDC2/T-cell co-cultures after restimulation with PMA and ionomycin in the presence of Golgi-plug and Golgi-stop. Shown are representative flow cytometry plots corresponding to the cumulative data depicted in Figure 2C (C) Proportions of $ICOS^+CXCR5^+$ T-cells in the different DC/T-cell co-cultures were determined at day 4. Shown are representative flow cytometry plots corresponding to the cumulative data depicted in Figure 2E (n=6). (D) Percentages of $PD\text{-}1^{hi}BCL6^{hi}$ cells in $ICOS^+CXCR5^+$, $ICOS^+CXCR5^-$ and $ICOS^-CXCR5^-$ T-cell subsets in the cDC2/T-cell co-cultures were determined via flow cytometry. Shown are representative flow cytometry plots corresponding to the cumulative data depicted in Figure 2F (n=6).

Figure E3: Lung cDC2 are the most potent inducers of Tfh-like cell polarization. DC subsets were purified from non-obstructed peritumoral lung resections and co-cultured with allogeneic naïve blood $CD4^+$ T-cells that were prelabeled with CFSE. (A) Proliferation of T-cells was assessed via flow cytometry at day 7. Shown are representative histograms of $CFSE^{lo}$ T-cell proportions present in the indicated co-cultures and combined data graph in which each symbol represents an individual donor (n=10). (B) Intracellular IFN-γ (n=10) staining of $ICOS^+PD\text{-}1^+$ (purple), $ICOS^-PD\text{-}1^+$ (orange), $ICOS^+PD\text{-}1^-$ (blue) and $ICOS^-PD\text{-}1^-$ (black) T-cell subsets in cDC2/T-cell co-cultures at day 7 after restimulation with PMA and ionomycin in the presence of Golgi-plug and Golgi-stop. Shown are representative flow cytometry plots and combined data graph in which each symbol represents an individual donor. (C) Percentages of $ICOS^+PD\text{-}1^+IFN\text{-}\gamma^+$ T-cells in cDC2/T-cell and cDC1/T-cell co-cultures were determined after 7 days. Each symbol represents an individual donor (n=10). $^{**}p<0.01$, $^{***}p<0.001$, Tukey's multiple comparison test (A and B) and Student *t*-test (C).

Figure E4: cDC2 from COPD GOLD II lungs display increased potential to promote Tfh-like cell skewing. (A), (B) and (C) cDC2 were isolated from COPD GOLD II peritumoral lung

tissues (n=7) and co-cultured with allogeneic naïve $CD4^+$ T-cells that were prelabeled with CFSE. Proportions of $ICOS^+PD\text{-}1^+$ T-cells (A) and $ICOS^+PD\text{-}1^+IL\text{-}21^+$ T-cells (B) were determined at day 7 and compared to cells from non-obstructed peritumoral lung tissues used in Figure 2 (n=10). Shown are representative flow cytometry plots corresponding to the cumulative data depicted in Figure 3A (E4A) and 3B (E4B) respectively. (C) Proliferation of T-cells (% of $CFSE^{lo}$ T-cells) was assessed via flow cytometry at day 7. Shown is combined data graph in which each symbol represents an individual donor. (D) $CD1c^+CD14^+$ fractions within cDC2 from non-obstructed control and COPDII peritumoral lung tissue used in the co-culture experiments presented in Figure 2 and 3. Show is the summary data graph (n=10 for control and n=7 for COPD). (E) Percentages of $ICOS^+PD\text{-}1^+$ Tfh-like cells in peritumoral lung tissue resections of COPD and non-obstructed control subjects determined via flow cytometry. Shown are representative flow cytometry plots corresponding to the cumulative data depicted in Figure 3C (n=6 for controls and n=5 for COPD subjects).

Figure E5: cDC2 exhibit a unique migratory pattern. (A) Surface levels of CXCR5, CXCR4 and EBI2 were measured on cDC2 and cDC1 from non-obstructed peritumoral lung resections via flow cytometry (n=8 for CXCR5, n=5 for CXCR4 and n=7 for EBI2). Shown are representative flow cytometry histograms for each marker and corresponding isotype. Cumulative data of this experiment depicted in Figure 4A. (B) Surface levels of CXCR5, CXCR4 and EBI2 were measured on cDC2 from non-obstructed and COPD peritumoral lung resections via flow cytometry (control n=8; and COPD n=4 for CXCR5, control n=5; and COPD n=3 for CXCR4 and control n=7; and COPD n=4 for EBI2). Shown is summary data graph for all the markers (mean MFI corrected for background intensity). (C) Surface EBI2 levels on $ICOS^+PD\text{-}1^+$ (purple), $ICOS^-PD\text{-}1^+$ (orange), $ICOS^+PD\text{-}1^-$ (blue) and $ICOS^-PD\text{-}1^-$ (black) T-cell subsets in the lung measured via flow cytometry. Shown are representative flow

cytometry histograms for EBI2 and isotype of corresponding cumulative data depicted in Figure 4B (n=10).

Supplemental Tables

Table S1: Single Cell cluster markers top 20 by logFC

Cluster	Gene	avg_logFC
1	FCER1A	2,088139734
1	CD1C	1,706769549
1	CCL17	1,449676397
1	HLA-DQB1	1,198897632
1	CD1E	1,159336889
1	HLA-DQA1	1,084527054
1	FCGR2B	1,068335054
1	CD1A	1,042954992
1	CLEC10A	1,027904208
1	CD1B	0,950553648
1	MS4A6A	0,930901312
1	HLA-DRB1	0,903968868
1	HLA-DRA	0,902474636
1	PKIB	0,890630909
1	CD86	0,829732946
1	C15orf48	0,82015284
1	SGK1	0,81219212
1	MNDA	0,812000223
1	GPR183	0,807344769
1	YWHAH	0,798773794
2	FN1	2,095765876
2	FABP4	1,596997079
2	MARCO	1,563296564
2	GPNMB	1,478726772
2	MSR1	1,390751001
2	MCEMP1	1,37408424
2	MRC1	1,368984707
2	CTSD	1,359952157
2	CCL18	1,351578234
2	FBP1	1,333490303
2	OLR1	1,215738999
2	APOC1	1,121526259
2	CTSB	1,106845823
2	LTA4H	1,067928201
2	LGALS3	1,05322345
2	GCHFR	1,044764711
2	VSIG4	0,960665094
2	CTSL	0,955551603
2	INHBA	0,955106343
2	FTL	0,95059228
3	HBG2	2,302686561

3	HBG1	2,027885733
3	AC104389.5	1,865440664
3	GAGE1	1,610717586
3	GTSF1	1,424267207
3	TOP2A	1,335903152
3	NMU	1,299328361
3	PRAME	1,280435628
3	HBE1	1,274461074
3	HIST1H1C	1,253113637
3	UQCRH	1,252614609
3	CKS1B	1,153736826
3	STMN1	1,131076794
3	PAGE5	1,129167523
3	KRT18	1,105038367
3	XAGE1A	1,088383961
3	TPX2	1,033839997
3	EPRS	1,024921962
3	CENPF	1,021810842
3	IFITM1	1,011736626
4	GZMB	3,575265882
4	JCHAIN	2,767735764
4	PLAC8	2,105195767
4	CCDC50	1,883419665
4	TCF4	1,859471292
4	C12orf75	1,831600843
4	IGKC	1,808955309
4	TCL1A	1,801589347
4	TSPAN13	1,716220583
4	CLEC4C	1,693808536
4	BCL11A	1,674993584
4	IRF4	1,637598991
4	UGCG	1,568753728
4	SELL	1,502616827
4	PPP1R14B	1,47257052
4	SOX4	1,456868998
4	HBB	1,438319472
4	ALOX5AP	1,389828099
4	CLIC3	1,361646152
4	SLC15A4	1,340439327
5	VCAN	1,879909516
5	THBS1	1,710398277
5	S100A8	1,707046345
5	S100A9	1,440827397
5	IL1B	1,339112206
5	EREG	1,241721323
5	FCN1	1,091242627
5	CD300E	1,050490024
5	CXCL8	1,011534339

5	APOBEC3A	0,876431337
5	SLC11A1	0,84018397
5	BTBD9	0,809890351
5	CNOT11	0,788145477
5	PCDH9	0,753261137
5	LYZ	0,72719212
5	SLC2A3	0,726358945
5	DOCK7	0,725081441
5	RPSAP48	0,719022886
5	AREG	0,716165035
5	NCALD	0,707815369
6	CCL5	3,094512646
6	CD3D	2,545536387
6	CD2	2,251160687
6	TRAC	2,199659021
6	TRBC2	2,065034272
6	CD3G	1,867353038
6	GZMA	1,743103623
6	CD96	1,737923673
6	SYNE2	1,699053241
6	LCK	1,622384641
6	CD52	1,53198628
6	IFNG	1,53013766
6	CLEC2D	1,491061473
6	CD69	1,481444892
6	TRBC1	1,454386996
6	RORA	1,405689794
6	MKI67	1,374739993
6	TNFAIP3	1,301620037
6	TRAT1	1,299873087
6	GNLY	1,295854049
7	FCGR3A	1,721454744
7	FCN1	1,572985976
7	TNFRSF1B	1,285868263
7	LYST	1,271273287
7	MTSS1	1,250671831
7	CTSS	1,235559792
7	SAT1	1,210844606
7	AIF1	1,180556797
7	APOBEC3A	1,117110701
7	LYN	1,090384191
7	COTL1	1,088225378
7	NAMPT	1,066627046
7	MS4A7	1,057457697
7	WARS	1,046454264
7	HCK	0,994740229
7	MAFB	0,95714909
7	CARD16	0,949365146

7	PECAM1	0,920995962
7	POU2F2	0,899423847
7	PSAP	0,899220709
8	C1orf54	2,502920156
8	S100B	2,215423608
8	CPVL	2,05870984
8	WDFY4	2,030191206
8	CPNE3	1,957136877
8	LGALS2	1,665749813
8	SNX3	1,646792957
8	CST3	1,629844392
8	NAPSB	1,60665153
8	IDO1	1,57189014
8	ID2	1,560949215
8	IRF8	1,50888726
8	CLNK	1,473985276
8	CCND1	1,407907195
8	SLAMF7	1,392130385
8	NAAA	1,374342149
8	CLEC9A	1,340110661
8	DNASE1L3	1,339190346
8	RAB7B	1,288662865
8	WFDC21P	1,286948554
9	SCGB3A2	3,795060405
9	SCGB1A1	3,752372645
9	SFTPB	3,513181643
9	SFTPC	3,410659195
9	SLPI	3,237610149
9	BPIFB1	3,006507765
9	SCGB3A1	2,988363079
9	CYB5A	2,353858175
9	PIGR	2,252972921
9	GPRC5A	2,087974649
9	SFTPA1	2,021757317
9	FMO2	1,990456688
9	SFTPA2	1,988487793
9	KRT19	1,877400103
9	FOLR1	1,797672424
9	CXCL17	1,749139084
9	TMC5	1,741303172
9	DNAH5	1,732458055
9	ELF3	1,708781385
9	STEAP4	1,691137143
10	VWF	2,563873467
10	MGP	2,98839516
10	SPARCL1	2,944658372
10	EPAS1	2,867006965
10	IL33	2,614155574

10	TM4SF1	2,581506323
10	CCL21	2,437221467
10	ABI3BP	2,381497238
10	MMRN1	2,356122626
10	ADIRF	2,300596205
10	CAV1	2,290802751
10	PTPRB	2,258068327
10	CTNNAL1	2,252002567
10	CALCRL	2,215405606
10	IGFBP7	2,213770782
10	VCAM1	2,174300302
10	GIMAP7	2,169786669
10	TNFSF10	2,098405801
10	EDN1	2,09597821
10	ADAMTS1	2,082354785
11	CCR7	2,974205214
11	BIRC3	2,682384903
11	LAMP3	2,493221552
11	CCL22	2,414283922
11	TBC1D4	1,811253495
11	IDO1	1,689907394
11	TXN	1,636759411
11	WFDC21P	1,598379937
11	KIF2A	1,572294609
11	DAPP1	1,556414637
11	CCL17	1,522183075
11	NUB1	1,422680026
11	IL7R	1,382598269
11	RASSF4	1,334039962
11	CSF2RA	1,324384725
11	MARCKS	1,322230231
11	CD274	1,307035179
11	C15orf48	1,273655846
11	MARCKSL1	1,269756605
11	BCL2A1	1,267413041
12	CXCL10	3,616408913
12	CCL8	2,755419177
12	GBP1	2,360339823
12	CXCL11	2,235367058
12	CXCL9	2,182283139
12	CCL2	1,808776529
12	C15orf48	1,544114364
12	GBP5	1,497176194
12	IFIT3	1,437316392
12	CALHM6	1,406032207
12	ISG15	1,385695314
12	APOBEC3A	1,376004478
12	STAT1	1,316194086

12	IDO1	1,26595354
12	PLEK	1,180306973
12	LAP3	1,173269394
12	GBP4	1,171045851
12	TFEC	1,025846406
12	ANKRD22	1,023264534
12	SLAMF7	1,021390851
13	HPGDS	3,269991728
13	CPA3	3,249401012
13	MS4A2	3,112447667
13	KIT	2,807435493
13	CD69	2,424658268
13	IL1RL1	2,357782247
13	TPSB2	2,277193757
13	TPSAB1	2,263245984
13	HPGD	2,104334302
13	HDC	2,085005909
13	RHEX	1,992779128
13	SLC18A2	1,987502805
13	RAB27B	1,930387753
13	VWA5A	1,920039685
13	SCGB1A1	1,772399364
13	RGS13	1,772384031
13	PTGS2	1,577393427
13	SLPI	1,501243584
13	ACSL4	1,487190145
13	EGR3	1,472376666
14	FOLR2	2,114128205
14	LYVE1	2,073485389
14	SELENOP	2,056837651
14	SLC40A1	1,998779877
14	RNASE1	1,980077253
14	CXCL3	1,714787741
14	MT1E	1,625695735
14	CD14	1,535402852
14	MT1X	1,51899883
14	CXCL2	1,510258367
14	MT1G	1,468134634
14	F13A1	1,36859711
14	MT2A	1,294103951
14	C3AR1	1,277064909
14	C1QA	1,274293948
14	CD163	1,271227942
14	MSR1	1,269660758
14	CXCL8	1,266401537
14	MAF	1,256446169
14	CCL4	1,238808215

Figure E1

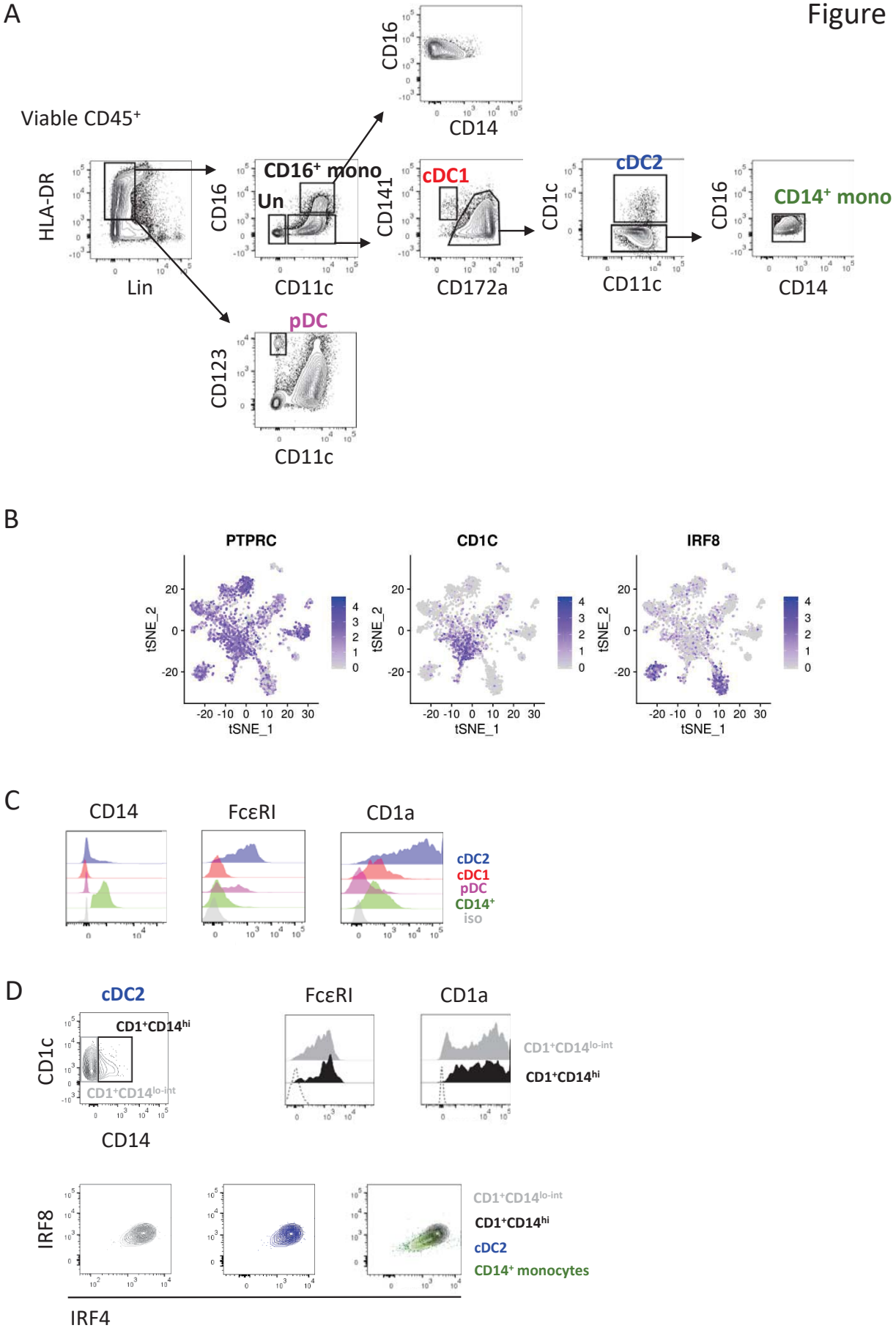
A
Viable CD45+
HLA-DR
Lin
CD16
CD14
CD16+ mono
Un
CD11c
CD141
cDC1
CD172a
CD1c
cDC2
CD11c
CD16
CD14+ mono
CD14
CD123
pDC
CD11c
B
PTPRC
CD1C
IRF8
tSNE_2
tSNE_1
C
CD14
FcεRI
CD1a
cDC2
cDC1
pDC
CD14+
iso
D
cDC2
CD1c
CD1+CD14hi
CD1+CD14lo-int
CD14
FcεRI
CD1a
CD1+CD14lo-int
CD1+CD14hi
IRF8
IRF4
CD1+CD14lo-int
CD1+CD14hi
cDC2
CD14+ monocytes

Figure E2

A

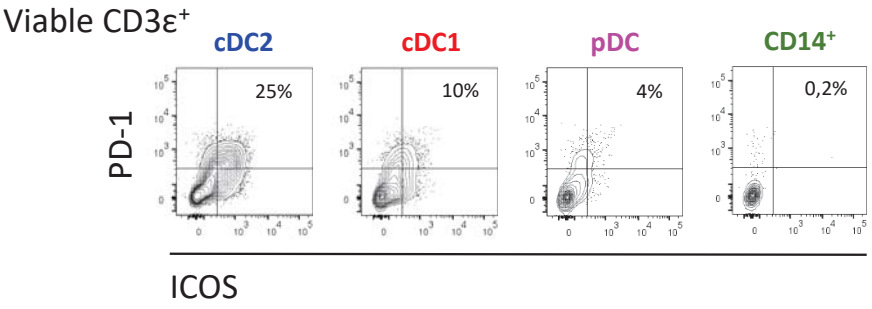

B

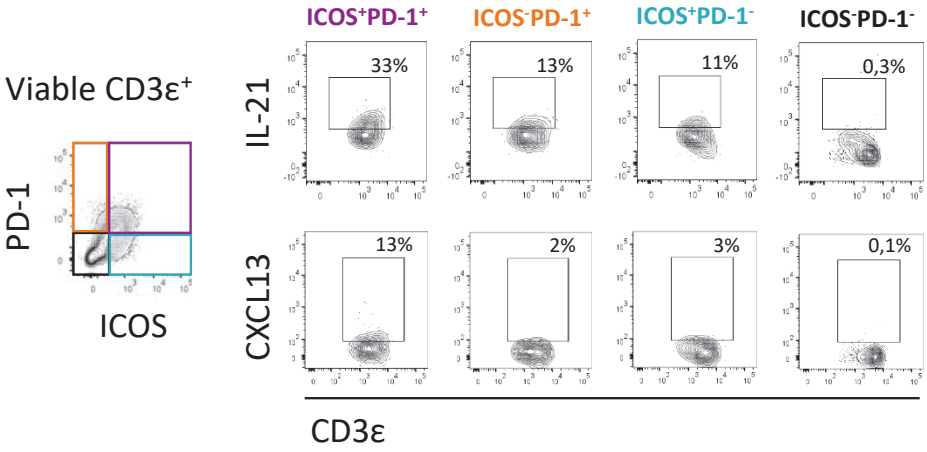

C

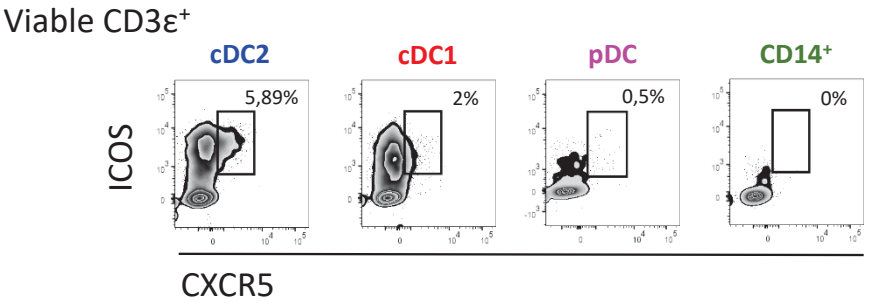

D

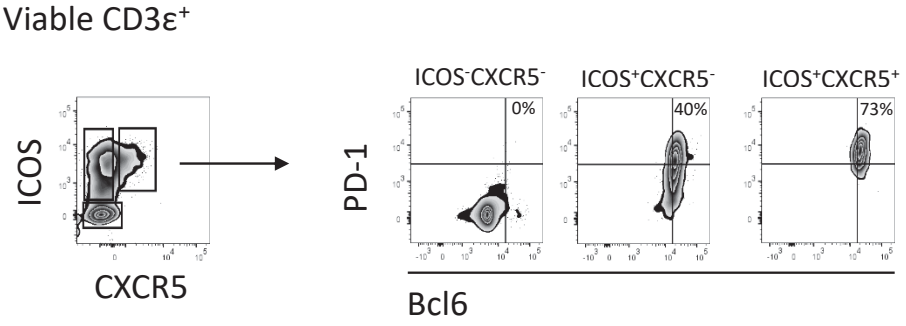

Figure E3

A

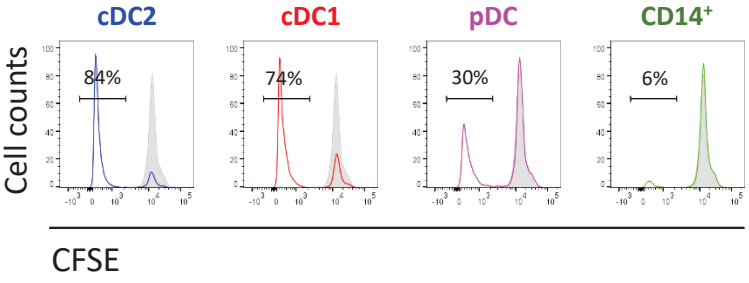

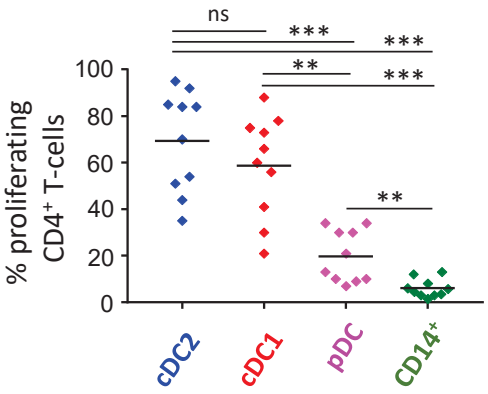

B

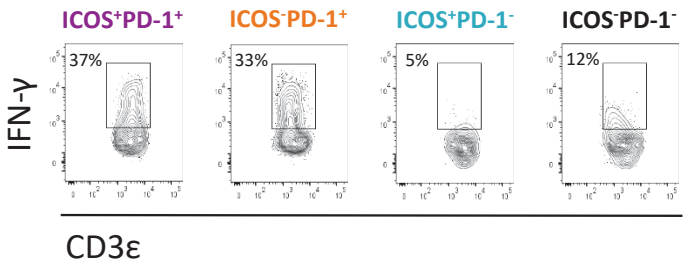

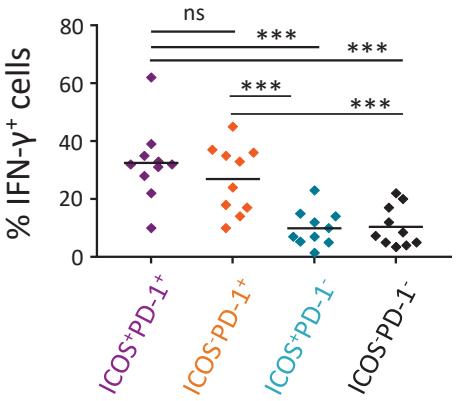

C

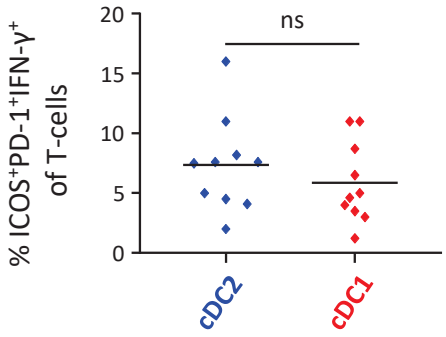

Figure E4

A

Viable CD3ε⁺

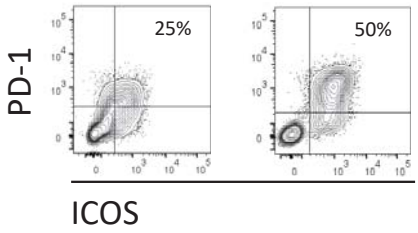

B

Viable CD3ε⁺PD-1⁺ICOS⁺

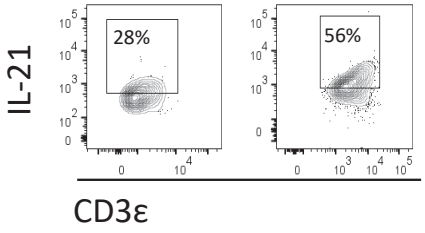

C

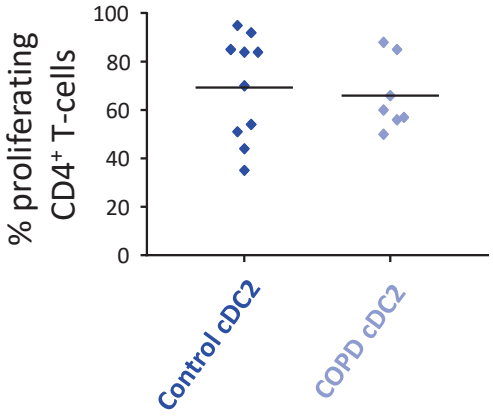

D

CD1c⁺CD14⁺ proportion

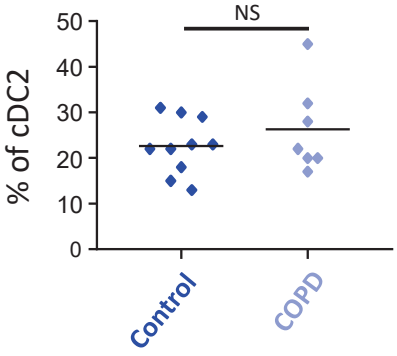

E

Viable CD3ε⁺ CD4⁺

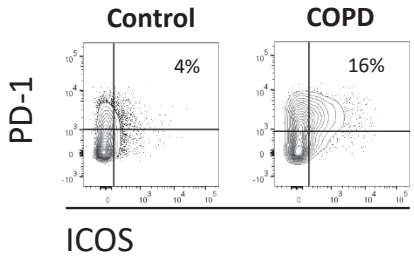

Figure E5

A

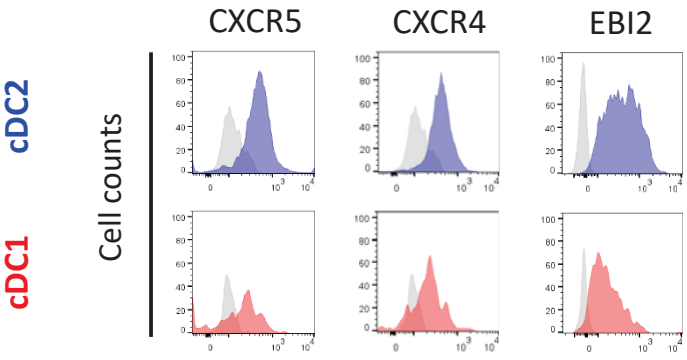

C

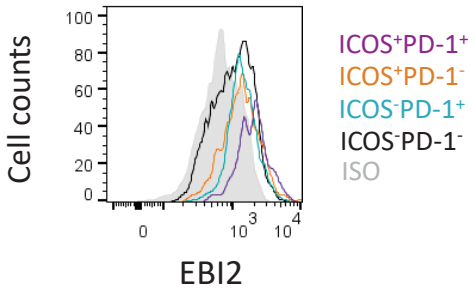

B